Manuscript prepared for Atmos. Chem. Phys.
with version 2014/09/16 7.15 Copernicus papers of the LaTeX class copernicus.cls.
Date: 13 February 2016

Potential sensitivity of photosynthesis and isoprene emission to direct radiative effects of atmospheric aerosol pollution

S. Strada[1,a] and N. Unger[1]

[1]School of Forestry and Environmental Studies, Yale University, New Haven, CT, USA
[a]now at: Laboratoire des Sciences du Climat et de l'Environnement, Gif-sur-Yvette, France

Correspondence to: S. Strada (susanna.strada@lsce.ipsl.fr)

Abstract. A global Earth system model is applied to quantify the impacts of direct anthropogenic aerosol effective radiative forcing on gross primary productivity (GPP) and isoprene emission. The impacts of different pollution aerosol sources (anthropogenic, biomass burning and non-biomass burning) are investigated by performing sensitivity experiments. The model framework includes all known light and meteorological responses of photosynthesis but uses fixed canopy structures and phenology. On a global scale, our results show that global land carbon fluxes (GPP and isoprene emission) are not sensitive to pollution aerosols, even under a global decline in surface solar radiation (direct+diffuse) by $\sim 9\,\%$. At a regional scale, GPP and isoprene emission show a robust but opposite sensitivity to pollution aerosols, in regions where forested canopies dominate. In eastern North America and Eurasia, anthropogenic pollution aerosols (mainly from non-biomass burning sources) enhance GPP by $+5$–$8\,\%$ on an annual average. In the north-western Amazon Basin and central Africa, biomass burning aerosols increase GPP by $+2$–$5\,\%$ on an annual average, with a peak in the north-western Amazon Basin during the dry-fire season ($+5$–$8\,\%$). The prevailing mechanism varies across regions: light scattering dominates in the eastern North America while reduction in direct radiation dominates in Europe and China. Aerosol-induced GPP productivity increases in the Amazon and central Africa include an additional positive feedback from reduced canopy temperatures in response to increases in canopy conductance. In Eurasia and north-eastern China, anthropogenic pollution aerosols drive a decrease in isoprene emission of $-2\,\%$ to $-12\,\%$ on an annual average. Future research needs to incorporate the indirect effects of aerosols and possible feedbacks from dynamic carbon allocation and phenology.

1 Introduction

Terrestrial gross primary productivity (GPP), the amount of carbon dioxide (CO_2) taken up every year from the atmosphere by plant photosynthesis, is the largest single flux in the carbon cycle and therefore plays a major role in global climate change. GPP is tightly connected to climatic variables (e.g., temperature, water, light) (Beer et al., 2010). In turn, terrestrial vegetation provides the main source of isoprene to the atmosphere, which controls the loading of multiple short-lived climate pollutants and greenhouse gases (ozone, methane, secondary aerosols). Isoprene production is closely linked to plant photosynthesis (Pacifico et al., 2009; Unger et al., 2013). Hence, both GPP and isoprene emission may be influenced by a change in surface solar radiation (SSR, the sum of the direct and diffuse radiation incident on the surface) and surface atmospheric temperature (SAT). Anthropogenic aerosols affect directly the Earth's radiation flux via: (a) scattering, which alters the partitioning between direct and diffuse radiation, increases the diffuse fraction of SSR and affects SAT (Wild, 2009); and (b) absorption, which reduces SSR and SAT (Ramanathan et al., 2001). Furthermore, aerosols may attenuate indirectly SSR by acting as cloud condensation nuclei, thus perturbing cloud cover and cloud properties (Rosenfeld et al., 2008).

In 1991, Mount Pinatubo (Philippines) injected 20 megatons of sulfur dioxide (SO_2) into the stratosphere causing a massive production of sulfate aerosols, with substantial impacts on climate, and on the water and carbon cycles (Jones and Cox, 2001; Gu et al., 2003; Trenberth and Dai, 2007). In the aftermath of the eruption, a loss in net global radiation at the TOA (Top Of the Atmosphere) and a concomitant cooling were observed, and ultimately led to drying (Trenberth and Dai, 2007). By efficiently scattering light, the volcanic sulfate aerosol production caused a significant increase in diffuse solar radiation. In 1991 and 1992, at two northern mid-latitude sites, Molineaux and Ineichen (1996) recorded an increase in clear-sky diffuse radiation by $+50\,\%$, compensated by a concomitant decrease in direct radiation of $-30\,\%$. Over the same period, in a deciduous forest in North-America, Gu et al. (2003) ascribed to increased diffuse radiation an enhancement in plant productivity of $+23$ and $+8\,\%$ in the two years following the Pinatubo eruption. On the global scale, enhancement in the terrestrial carbon sink was proposed as one of the main drivers of the sharp and rapid decline in the rate of atmospheric CO_2 rise observed in the post-Pinatubo period, which resulted in a decrease of $3.5\,\mathrm{ppmv}$ by 1995 in atmospheric CO_2 (Keeling et al., 1995; Jones and Cox, 2001; Gu et al., 2003). The "Mount Pinatubo experiment" suggested a possible global response of terrestrial vegetation to the "diffuse fertilization effect" (DFE). Observational and theoretical studies show that plant productivity is more efficient under multi-directional diffuse rather than direct light because shaded non-light-saturated leaves increase their photosynthetic rate (Gu et al., 2002).

The DFE on plant photosynthesis has been extensively observed at ecosystem scale under cloudy skies (e.g., Gu et al., 2002; Niyogi et al., 2004; Cheng et al., 2015) and a chronic aerosol loading (e.g., Gu et al., 2003; Oliveira et al., 2007; Cirino et al., 2014) in diverse ecosystems (rainforest, deciduous and needleleaf forest, crop- and grasslands). The main conclusions of these studies are:

(1) DFE prevails in complex and closed canopies, such as forests (Niyogi et al., 2004; Kanniah et al., 2012); (2) intermediate aerosol optical depth (AOD) enhances plant productivity, while high AOD ($>$ 2–3) reduces carbon uptake rate because of a large reduction in direct radiation (Oliveira et al., 2007; Artaxo et al., 2013; Cirino et al., 2014). An ecosystem-scale measurement study in a European mixed needleleaf and deciduous forest reported increased isoprene emissions under conditions of higher diffuse light (Laffineur et al., 2013).

A few modeling studies have investigated aerosol-induced effects on plant productivity. Regional- and daily-scale assessments have been performed over: the Yellow River region (China), selecting a period of five days (Steiner and Chameides, 2005); and over the eastern United States, selecting two growing seasons (Matsui et al., 2008). Results in both studies are consistent with the main conclusions of the local observational studies. Steiner and Chameides (2005) demonstrated the importance of both aerosol-induced radiative (i.e., change in light amount and its partitioning) and thermal (i.e., change in surface temperature) effects on plant transpiration and productivity. However, these studies focus on short time periods and a limited number of ecosystems using offline models with single-layer canopy schemes.

By applying a multi-layer canopy scheme in an offline modeling framework (i.e., aerosol, radiative transfer and land-surface models are coupled offline), Rap et al. (2015) performed a regional- and decadal-scale assessment of aerosol-induced effects on plant productivity in the Amazon basin from 1998 to 2007. The authors specifically focused on biomass burning aerosols (BBAs) and quantified that BBAs increase the annual mean diffuse light and net primary production (NPP) by, respectively, $\sim 5\,\%$ and $\sim 2.5\,\%$. Deforestation fires play a key role and drive $\sim 40\,\%$ of the estimated changes in light and photosynthesis. Moreover, Rap et al. (2015) assessed that in the Amazon basin during 1998–2007 the DFE (a) was larger than the CO_2 fertilization effect, and (b) it could counteract the negative effect of droughts on land carbon fluxes.

A global-scale assessment of the aerosol-induced effects on the carbon cycle was performed by Mercado et al. (2009) using an offline land-surface model with a multi-layer canopy scheme. The authors concluded that DFE enhanced the global land carbon sink by $+23.7\,\%$ over the 20th century, under an overall radiation (direct+diffuse) change of $+9.3\,\%$. Mercado et al. (2009) reconstructed historical SSR using radiative transfer calculations and a global climate dataset for the "global dimming" (period 1950–1980) and the "global brightening" period (after 1990s) (Wild, 2009, 2012; Streets et al., 2009). Recently, Chen and Zhuang (2014) applied an atmospheric radiative transfer module coupled with a terrestrial ecosystem model to quantify aerosol direct radiative effects on global terrestrial carbon dynamics during 2003–2010. Using transient atmospheric CO_2 and prognostic leaf area index (LAI, one-sided green leaf area per unit ground area), the authors evaluated aerosol impacts on plant phenology, thermal and hydrological conditions as well as solar radiation. Chen and Zhuang (2014) estimated that, on a global scale, aerosols enhance GPP by $4.9\,\mathrm{Pg\,C\,yr^{-1}}$

and slightly affect respiration. Chen and Zhuang (2014) accounted for all atmospheric aerosols and they did not target anthropogenic pollution aerosols.

Understanding all anthropogenic factors that influence the land carbon cycle is crucial to better manage terrestrial vegetation and to any effort to mitigate climate change by stabilizing atmospheric CO_2 concentrations. In the present study, we quantify the sensitivity of GPP and isoprene emission to the direct radiative effects of a realistic present-day pollution aerosol loading. Using a global Earth system model that represents vegetation–oxidant–aerosol–climate coupling, we perform sensitivity simulations to isolate the impact of the present-day pollution aerosols on GPP and isoprene emission. We tackle the direct aerosol effect only (absorption + scattering) and its impact on SSR and SAT that affects land carbon fluxes. Aerosol indirect effects on cloud properties are not addressed in this study due to the large uncertainties (Boucher et al., 2013; Myhre et al., 2013a). This study focuses on GPP because it is the first step in the long-term storage of atmospheric CO_2 in the living tissues of plants and is directly affected by solar radiation. We do not address aerosol effects on other land carbon cycle fluxes (e.g., respiration, net ecosystem exchange). We employ the effective radiative forcing (ERF) concept metric introduced in the IPCC AR5 in which all physical variables are allowed to respond to the direct aerosol–radiation perturbations except for those concerning the ocean and sea ice (Myhre et al., 2013b). The inclusion of these rapid adjustments in the ERF metric allows us to investigate the multiple aerosol-induced concomitant meteorological impacts on the biosphere.

Section 2 describes the global Earth system model tool (NASA ModelE2-YIBs) and the experimental design. In Sect. 3, we evaluate simulated present-day atmospheric aerosols and GPP against global observational datasets including AOD from the Moderate Resolution Imaging Spectroradiometer (MODIS) and global gridded GPP that was generated using data orientated diagnostic upscaling of site-derived GPP from FLUXNET (Beer et al., 2010; Bonan et al., 2011; Jung et al., 2011). In addition, we present the analysis of results from the sensitivity simulations. In Sect. 4, we discuss the results and summarize conclusions.

2 Methodology

2.1 Global Earth system model: NASA ModelE2-YIBs

We apply the NASA GISS ModelE2 global chemistry-climate model at $2^\circ \times 2.5^\circ$ latitude by longitude horizontal resolution with 40-vertical layers extending to $0.1\,\mathrm{hPa}$ (Schmidt et al., 2014). The Yale Interactive Terrestrial Biosphere Model (YIBs) is embedded inside NASA ModelE2 in a framework known as NASA ModelE2-YIBs (Unger et al., 2013). The global climate model provides the meteorological drivers for the vegetation physiology. The land-surface hydrology submodel provides the grid cell level soil characteristics to the vegetation physiology. The model framework fully integrates the land biosphere–oxidant–aerosol system such that these components interact with each other and with the physics of the climate model. On-line oxidants affect aerosol production and

on-line aerosols provide surfaces for chemical reactions and influence photolysis rates. The chemistry and aerosol schemes and their coupling have been well documented and extensively compared with observations and other global models (e.g., Bell et al., 2005; Bauer et al., 2007; Koch et al., 2006; Koch and Del Genio, 2010; Unger, 2011; Myhre et al., 2013a; Shindell et al., 2006, 2013a, b; Stevenson et al., 2013).

The aerosol package includes mass-based simulation of sulfate, nitrate and sea salt (e.g., Koch et al., 2006), carbonaceous aerosols (black carbon, BC, and primary organic matter, OC) (Koch and Hansen, 2005), mineral dust (Miller et al., 2006), and biogenic secondary organic aerosol (BSOA) (Tsigaridis and Kanakidou, 2007). The model assumes log-normal size distributions with effective radii: $0.2\,\mu\mathrm{m}$ (sulfate); $0.3\,\mu\mathrm{m}$ (nitrate); $0.1\,\mu\mathrm{m}$ (BC); $0.3\,\mu\mathrm{m}$ (OC). Sea salt aerosols are represented by two size bins with effective radii of 0.44 and $5\,\mu\mathrm{m}$. Mineral dust aerosols are tracked in four size bins, ranging from 0.1 to $10\,\mu\mathrm{m}$, and can be coated by sulfate and nitrate aerosols. Hygroscopic aerosols (sulfates, nitrates, sea salt and organic carbon) increase in size with increasing relative humidity, which increases the aerosol scattering efficiency and radiative forcing (Schmidt et al., 2006).

The direct effect interaction between aerosols and radiation is reproduced by the on-line (two-way coupled) mode: aerosol fields are simulated at each model time step ($30\,\mathrm{min}$) and influence the simulated short and longwave radiation through scattering and absorption in the radiation submodel, which in turn influences the climate dynamics. Thus, aerosols induce (a) changes in simulated diffuse and direct photosynthetically active radiation (PAR, spectral range of surface visible solar radiation, 400–$700\,\mathrm{nm}$, used by plants to photosynthesize) that are passed from the radiation submodel to the vegetation model; and (b) rapid adjustment changes in meteorology (temperature, precipitation, circulation) that are passed from the model's atmosphere and land surface to the vegetation model.

2.1.1 The Yale Interactive Terrestrial Biosphere model (YIBs)

The vegetation structure describes eight plant functional types (PFTs): tundra, grassland, shrubland, deciduous broadleaf forest, savannah, tropical rainforest, evergreen needleleaf forest, and cropland. The PFT-specific vegetation cover fraction and LAI are the standard atlas-based distribution in NASA GISS ModelE2 (Schmidt et al., 2014). LAI for each PFT is prescribed according to regular seasonal sinusoidal variation between PFT-specific minimum and maximum seasonal LAI values that is insensitive to climate drivers or carbon balances (Rosenzweig and Abramopoulos, 1997; Friend and Kiang, 2005). Each model PFT fraction in the vegetated part of each grid cell represents a single canopy. The canopy radiative transfer scheme assumes a closed canopy and distinguishes vertically canopy layers into sunlit and shaded leaves, as well as the different contributions from direct and diffuse PAR (from the climate model's radiation scheme) at the leaf level (Spitters et al., 1986). The leaf-level carbon and water fluxes are scaled up to the canopy level by integrating over each canopy layer, using an adaptive number of layers (typically 2–16) (Friend and Kiang, 2005).

After upscaling from leaf to canopy, the carbon and water fluxes are exchanged with the atmosphere on the 30–minutes physical integration time step of the global climate model.

The vegetation biophysical fluxes are calculated using the well-established leaf model of photosynthesis (Farquhar et al., 1980; Von Caemmerer and Farquhar, 1981) and the stomatal conductance model of Ball and Berry (Ball et al., 1987). In the leaf model, the rate of net CO_2 uptake in the leaves of C_3 plants is the result of three competing processes: J_c, the carboxylation-limited rate; J_e, the electron transport-limited photosynthesis rate; and J_s, the export-limited rate to use photosynthesis products. The coupled photosynthesis, stomatal conductance and diffusive CO_2 flux transport equations are solved analytically at the leaf level using a cubic function in the net carbon assimilation rate. Isoprene emission is calculated as a function of J_e, intercellular and atmospheric CO_2 and canopy temperature (Unger et al., 2013).

As theoretical and observational studies have demonstrated, the aerosol effect on plant photosynthesis strongly depends on the canopy separation into sunlit and shaded leaves. These two parts of the canopy have different responses to the change in light partitioning driven by aerosols (Knohl and Baldocchi, 2008). Under low PAR, both shaded and sunlit leaves are in a light-limited environment (J_e controls the photosynthesis rate). Under high PAR, sunlit leaves are light-saturated and in a Rubisco-limited environment (J_c controls the photosynthesis rate), while shaded leaves are in a light-limited environment (J_e). Hence, sunlit canopy photosynthesis depends on both direct and diffuse light, and on both J_c and J_e photosynthesis rates; while shaded canopy photosynthesis is directly influenced by diffuse light and mainly depends on the J_e photosynthesis rate. The aerosol light-scattering directly influences J_e, hence it mainly affects shaded leaves (Matsui et al., 2008; Chen and Zhuang, 2014).

Linkages between vegetation and atmospheric aerosols are extremely complex. This version of the land carbon cycle model captures the meteorological (light, temperature, relative humidity, precipitation) responses of photosynthesis. The use of fixed canopy structures and phenology means that leaf mass is not driven by photosynthetic uptake of CO_2 and a closed carbon cycle is not simulated. Thus, the simulated GPP and isoprene emission responses may be underestimated because the LAI is insensitive to CO_2 uptake and climate. The objectives here are to examine the meteorological responses in detail and to offer a benchmark for future research that will incorporate additional feedbacks from dynamic LAI and phenology. For example, aerosol-induced effects on light and surface temperature may alter (i) the onset and shutdown dates of photosynthesis and growing season length (Yue et al., 2015a), (ii) the carbon allocation, LAI and tree height that provide a feedback to GPP (Yue et al., 2015b).

2.2 Simulations

The atmosphere-only configuration of NASA ModelE2-YIBs is used to perform a control simulation ("SimCTRL") representative of the present-day ($\sim$ 2000s). Prescribed decadal average monthly-

varying sea surface temperature (SST) and sea ice observations for 1996–2005 from the HadSST dataset (Rayner et al., 2006) provide the lower boundary conditions for the global climate model. The present day trace gas and aerosol emissions are prescribed to year 2000 values from the historical inventory developed for IPCC AR5 (Lamarque et al., 2010). Atmospheric levels of long-lived greenhouse gases are prescribed to: $CO_2 = 370\,\mathrm{ppmv}$; $CH_4 = 1733\,\mathrm{ppbv}$ in Southern Hemisphere and $1814\,\mathrm{ppbv}$ in Northern Hemisphere; $N_2O = 316\,\mathrm{ppbv}$. A set of three sensitivity perturbation simulations are performed that selectively remove anthropogenic short-lived gas-phase precursor and primary aerosol emissions:

(a) all anthropogenic emissions, including biomass burning, are removed in "SimNOant";

(b) only biomass burning emissions are removed in "SimNObb";

(c) all industrial emissions, which means all anthropogenic emissions except biomass burning emissions (e.g., industry, power generation, road vehicles; hereafter, we refer to these emissions as "non-biomass burning emissions"), are removed in "SimNOind".

The control and sensitivity simulations are run for 32 model years recycling the year 2000 boundary conditions every year but allowing the changes in atmospheric aerosol composition to influence meteorology and the land biosphere. By prescribing SSTs and sea ice cover at climatological values, while letting all other physical components of the Earth system to respond until reaching steady state, we capture short-term response of the land surface climate to the aerosol radiation perturbation. This fixed-SST technique allows us to compute ERF, the forcing metric that accounts for rapid tropospheric adjustments and better characterizes drivers in the troposphere (e.g., aerosols) (Myhre et al., 2013b). Hence, the fixed-SST technique enables us to analyze multiple meteorological effects of the direct aerosol–radiation interactions. The long run-time is necessary to allow the fast land and atmosphere climatic feedbacks to respond to the aerosol perturbations and the TOA radiation fluxes to equilibrate. Integrations of 32 model years are completed for all simulations (control and sensitivity runs). The global atmospheric oxidant–aerosol composition usually takes about 2 years to spin-up, while the atmospheric dynamics and land–surface climate takes about 10 years to reach steady–state due to an imposed aerosol radiative forcing. Therefore, we discard the first 12 model run years as spin-up. The remaining 20 model run years are averaged for analysis. Twenty model years of data are necessary such that any aerosol-driven variable differences between the control and sensitivity simulations are statistically significant relative to internal climate model variability. Our goal is to isolate the effects of aerosol pollution on the land biospheric fluxes. Therefore, we compute the absolute differences in X variable as: $\Delta X = X_{\mathrm{ctrl}} - X_{\mathrm{sens}}$. Percentage changes in X are calculated relative to the control experiment (i.e., $\Delta_{\%} X = \Delta X / X_{\mathrm{ctrl}} \times 100$) and, for selected variables, are gathered in the Supplementary Material. Applying the same methodology, we compute absolute and percentage differences in annual and seasonal averages over selected regions. Hereafter, we define

"significant" all absolute/percentage changes that are statistically significant at the $95\,\%$ confidence level.

3 Results

3.1 Evaluation of present-day control simulation

Present-day values of global mean aerosol column burden (ACB) and ERF for aerosol–radiation interactions (i.e., aerosol direct effect) are presented by component in Table 1 and 2. The IPCC AR5 provides RF (not ERF) by single aerosol species (Boucher et al., 2013; Myhre et al., 2013b). NASA ModelE2-YIBs ERF values for single aerosol species are consistent with the AR5 RF ranges. Nitrate ERF is on the lower bound of the AR5 RF range (-0.30 to $-0.03\,\mathrm{W\,m^{-2}}$). ERFs of sulfate, BC from industrial sources and SOAs fall into the AR5 RF ranges (respectively: -0.60 to $-0.20\,\mathrm{W\,m^{-2}}$, $+0.05$ to $+0.80\,\mathrm{W\,m^{-2}}$, and -0.27 to $-0.20\,\mathrm{W\,m^{-2}}$). OC from industrial sources and BBAs show ERFs consistent with the AR5 RF values ($\mathrm{OC_{ind}}$: $-0.09\,\mathrm{W\,m^{-2}}$, BBAs: $0.00\,\mathrm{W\,m^{-2}}$). Based on a combination of methods (i.e., global aerosol models and observation-based methods), the AR5 report estimates the total ERF due to aerosol-radiation interactions: -0.45 (-0.95 to $+0.05$) $\mathrm{W\,m^{-2}}$; in AR5, the best total RF estimate of the aerosol–radiation interaction is: -0.35 (-0.85 to $+0.15$) $\mathrm{W\,m^{-2}}$ (Myhre et al., 2013b). The total ERF is computed in NASA ModelE2-YIBs as the arithmetic mean of all anthropogenic aerosol components (i.e., sulfate, nitrate, OC and BC from both industrial and biomass burning sources, SOA and dust). The NASA ModelE2-YIBs estimates a total ERF due to aerosol-radiation interactions of -0.34 (-0.76 to $+0.18$) $\mathrm{W\,m^{-2}}$, at the low end of the IPCC AR5 range.

Similarly to the aerosols, the present-day land carbon fluxes are in good agreement with previous estimates (Table 3). Simulated global annual GPP ($116.0\,\mathrm{Pg\,C\,yr^{-1}}$) is in reasonable agreement with current understanding of the present-day carbon cycle budget (based on FLUXNET: $123 \pm 8\,\mathrm{Pg\,C\,yr^{-1}}$, Beer et al., 2010; based on MODIS: $109.29\,\mathrm{Pg\,C\,yr^{-1}}$, Zhao et al., 2005; based on the Eddy Covariance-Light Use Efficiency model: $110.5 \pm 21.3\,\mathrm{Pg\,C\,yr^{-1}}$, Yuan et al., 2010). The global isoprene source is $402.8\,\mathrm{Tg\,C\,yr^{-1}}$, which is at the low end of the range of previous global estimates (e.g., 400–$700\,\mathrm{Tg\,C\,yr^{-1}}$, Guenther et al., 2006. However, a recent study suggests a larger range of 250–$600\,\mathrm{Tg\,C\,yr^{-1}}$ (Messina et al., 2015). The photosynthesis-based isoprene emission models tend to estimate a lower global isoprene source than empirical models because the scheme intrinsically accounts for the effects of plant water availability that reduce isoprene emission rates (Unger et al., 2013).

3.1.1 Aerosol Optical Depth (AOD)

We use the quality assured Terra MODIS Collection 5 (C5.1) monthly mean product (Level 3), a globally gridded dataset at $1^\circ \times 1^\circ$ resolution re-gridded to $2^\circ \times 2.5^\circ$ resolution for comparison with

the global model. To infer clear-sky (non cloudy) aerosol properties in part of the visible and shortwave infrared spectrum, MODIS C5.1 relies on two algorithms depending on surface reflectance: (1) the Dark Target (DT) algorithm, under conditions of low surface reflectance (e.g., over ocean, vegetation) (Levy et al., 2010); (2) the Deep Blue (DB) algorithm, designed to work under high surface reflectance, such as over desert regions (Hsu et al., 2004; Shi et al., 2014). To cover both dark and bright surfaces, we merge the DT and DB AOD products (i.e., DT missing data are filled in with DB values). We use MODIS TERRA C5.1 AOD data from 2000 to 2007 because DB AOD data are only available for this period due to calibration issues (Shi et al., 2014). The MODIS instrument also measures the fine model weighting (ETA) at $550\,\mathrm{nm}$, consequently the fine-mode AOD can be computed as: fine-AOD = AOD $\times$ ETA, where fine-AOD is the fraction of the AOD contributed by fine mode sized particles (i.e., effective radius $\ll 1.0\,\mu\mathrm{m}$) (Levy et al., 2010; Bian et al., 2010). Quantitative use of MODIS fine-AOD is not appropriate because fine-mode aerosols play a main role in the scattering process (Levy et al., 2010).

NASA ModelE2-YIBs provides separately all-sky and clear-sky AOD diagnostics; we focus on clear-sky output since that is more comparable to the spaceborne observations. The model coarse-mode (PM_{10}, atmospheric particulate matter with diameter $< 10\,\mu\mathrm{m}$) AOD includes all simulated aerosol species (sulfate, nitrate, organic and black carbon, SOA, sea salt and mineral dust); the model fine-mode ($PM_{2.5}$, atmospheric PM with diameter $< 2.5\,\mu\mathrm{m}$) AOD accounts for all simulated aerosol species except sea salt and dust.

Figure 1 compares the spatial distribution of annual and seasonal (boreal summer and winter) mean coarse-mode AOD in NASA ModelE2-YIBs (control present-day simulation) with observations from the MODIS satellite instrument (averaged over 2000–2007). Model global mean coarse-mode AODs are consistent with MODIS AOD global means. NASA ModelE2-YIBs reproduces strong biomass burning and dust episodes over Africa. In contrast, on both annual and seasonal averages the model underestimates the optical thickness of the aerosol layer over China and India, which is likely related to dust. The model's underestimate of Asian dust should not influence the focus of this study, to assess the impacts of anthropogenic pollution aerosols on the land carbon fluxes. The spatial and temporal distribution of fine-mode aerosols in NASA ModelE2-YIBs is consistent with MODIS observations (Fig. 2). In general, the model shows a slightly higher fine-aerosol layer compared to MODIS (e.g., over Europe, India and South America). Over China, model fine-AOD distribution is consistent with MODIS on the annual average; however, the model does not show the seasonal variability that MODIS observes. To quantify the model evaluation, on an annual average the NASA ModelE2-YIBs coarse-mode AOD global means present an acceptable correlation with the MODIS AOD global means ($R = 0.7$, $R^2 = 0.5$ and $RMSE = 0.05$, Table 4). Between boreal summer and winter, boreal summer shows the best model performance ($R = 0.8$, $R^2 = 0.6$ and $RMSE = 0.06$, Table 4). During boreal winter, outside the growing season, the NASA ModelE2-

YIBs overestimates coarse-mode AODs. Since quantitative use of MODIS fine-AOD is not recommended, we do not quantify model performance for fine-mode AODs.

3.1.2 Gross Primary Productivity (GPP)

In Fig. 3, we compare the spatial distribution of annual and seasonal (boreal summer and winter) mean GPP in NASA ModelE2-YIBs model (control present-day simulation) with a global FLUXNET-derived GPP product (averaged over 2000–2011). The model is consistent with the broad spatio-temporal variability in FLUXNET-derived GPP. We find a weaker annual and seasonal signal in the model GPP over the cerrado area in central South-America. However, since the FLUXNET-derived GPP product mainly relies on the availability of FLUXNET sites, which are densely distributed in temperate zone not in the tropics, FLUXNET-derived GPP may be biased over central South-America. On an annual average the NASA ModelE2-YIBs GPP highly correlates with the FLUXNET-derived GPP ($R = 0.9$, $R^2 = 0.7$, $RMSE = 1.0$, Table 4). Between boreal summer and winter, boreal winter presents the best model performance ($R = 0.9$, $R^2 = 0.9$ and $RMSE = 1.1$, Table 4). Recently, Yue and Unger (2015) performed a site-level evaluation of the YIBs model over 145 sites for different PFTs. Depending on PFT, GPP simulation biases range from $-19\,\%$ to $+7\,\%$. For monthly-average GPP, among the 145 sites, 121 have correlations higher than 0.8. High correlations (> 0.8) are mainly achieved at deciduous broadleaf and evergreen needle leaf sites; crop sites show medium correlation (~ 0.7).

3.2 Aerosol pollution changes in sensitivity simulations

3.2.1 Global-scale

Table 1 shows the aerosol column burden (ACB) by component in the control and the three sensitivity simulations. Anthropogenic pollution emissions (SimCTRL−SimNOant) contribute $0.85\,\mathrm{mg\,m^{-2}}$ to sulfate ACB ($36\,\%$ of the total sulfate burden due to both anthropogenic and natural emissions), $4.47\,\mathrm{mg\,m^{-2}}$ to nitrate ACB ($87\,\%$) and $0.99\,\mathrm{mg\,m^{-2}}$ to SOA ACB ($72\,\%$). Biomass burning emissions (SimCTRL−SimNObb) contribute $1.62\,\mathrm{mg\,m^{-2}}$ to nitrate ACB ($31\,\%$) and $0.23\,\mathrm{mg\,m^{-2}}$ to SOA ACB ($17\,\%$), while they do not significantly contribute to sulfate ACB. Non-biomass burning emissions (SimCTRL−SimNOind) contribute $0.89\,\mathrm{mg\,m^{-2}}$ to sulfate ACB ($37\,\%$), $3.69\,\mathrm{mg\,m^{-2}}$ to nitrate ACB ($72\,\%$) and $0.47\,\mathrm{mg\,m^{-2}}$ to SOA ACB ($34\,\%$). For carbonaceous aerosols, anthropogenic pollution emissions contribute $1.45\,\mathrm{mg\,m^{-2}}$ to the total OC ACB ($0.48\,\mathrm{mg\,m^{-2}}$ from non-biomass burning, $\mathrm{OC_{ind}}$, and $0.97\,\mathrm{mg\,m^{-2}}$ from biomass burning, $\mathrm{OC_{bb}}$) and $0.26\,\mathrm{mg\,m^{-2}}$ to the total BC ACB ($0.17\,\mathrm{mg\,m^{-2}}$ from non-biomass burning, $\mathrm{BC_{ind}}$, and $0.09\,\mathrm{mg\,m^{-2}}$ from biomass burning, $\mathrm{BC_{bb}}$). Non-biomass burning emissions contribute $0.15\,\mathrm{mg\,m^{-2}}$ to $\mathrm{OC_{bb}}$ ACB ($15\,\%$) and $0.01\,\mathrm{mg\,m^{-2}}$ to $\mathrm{BC_{bb}}$ ACB ($15\,\%$).

Table 2 presents, by aerosol component, the ERF for aerosol-radiation interactions due to anthropogenic pollution, biomass burning and non-biomass burning emissions. Anthropogenic pollution emissions contribute $-0.31\,\mathrm{W\,m^{-2}}$ to sulfate ERF ($40\,\%$ of the total sulfate ERF due to both anthropogenic and natural emissions), $-0.38\,\mathrm{W\,m^{-2}}$ to nitrate ERF ($85\,\%$) and $+0.10\,\mathrm{W\,m^{-2}}$ to SOA ERF ($63\,\%$). Biomass burning emissions contribute $-0.14\,\mathrm{W\,m^{-2}}$ to nitrate ERF ($30\,\%$) and $-0.03\,\mathrm{W\,m^{-2}}$ to SOA ERF ($16\,\%$), while they do not significantly contribute to sulfate ERF. Non-biomass burning emissions contribute $-0.30\,\mathrm{W\,m^{-2}}$ to sulfate ERF ($40\,\%$), $-0.31\,\mathrm{W\,m^{-2}}$ to nitrate ERF ($70\,\%$) and $-0.05\,\mathrm{W\,m^{-2}}$ to SOA ERF ($29\,\%$). For carbonaceous aerosols, anthropogenic pollution emissions contribute $-0.17\,\mathrm{W\,m^{-2}}$ to the total OC ERF ($-0.06\,\mathrm{W\,m^{-2}}$ from non-biomass burning, $\mathrm{OC_{ind}}$, and $-0.11\,\mathrm{W\,m^{-2}}$ from biomass burning, $\mathrm{OC_{bb}}$) and $+0.30\,\mathrm{W\,m^{-2}}$ to the total BC ERF ($+0.18\,\mathrm{W\,m^{-2}}$ from non-biomass burning, $\mathrm{BC_{ind}}$, and $+0.12\,\mathrm{W\,m^{-2}}$ from biomass burning, $\mathrm{BC_{bb}}$). Non-biomass burning emissions contribute $-0.01\,\mathrm{W\,m^{-2}}$ to $\mathrm{OC_{bb}}$ ERF ($9\,\%$) and $+0.02\,\mathrm{W\,m^{-2}}$ to $\mathrm{BC_{bb}}$ ERF ($11\,\%$).

3.2.2 Five key regions

Beyond the global results, our simulations reveal five strongly sensitive regions that correspond to important sources of aerosol pollution: eastern North-America, Eurasia, north-eastern China, the north-western Amazon Basin and central Africa (green boxes on Fig. 4). Besides a substantial contribution to primary aerosol (PA) sources (i.e., BC and OC), all selected regions considerably contribute to secondary aerosol (SA) sources such as sulfate, nitrate and SOA (Table S1 for ACB and Table S2 for ERF in the Supplementary Material). We focus on SAs since, being finer than PAs, they play a key role in scattering and may trigger DFE.

In terms of aerosol burden, in the five key regions, nitrate is the dominant aerosol source, with a larger contribution from non-biomass burning compared to biomass burning emissions. Sulfate source is mainly governed by non-biomass burning emissions, except in central Africa where biomass burning emissions importantly contribute to sulfate ACB. For SOA source, both biomass and non-biomass burning emissions feed SOA ACB, with a larger contribution from biomass burning in central Africa.

Eastern North America and Eurasia share a similar contribution to nitrate ACB ($\sim$ 14–$15\,\mathrm{mg\,m^{-2}}$; $\sim 93\,\%$) and ERF (-1.2–$1.3\,\mathrm{mg\,m^{-2}}$; $\sim 94\,\%$) due to anthropogenic emissions, with the largest input from non-biomass burning emissions (ACB: $12.7\,\mathrm{mg\,m^{-2}}$; ERF: $-1.1\,\mathrm{mg\,m^{-2}}$, $\sim 80\,\%$) compared to biomass burning emissions (ACB: $3.4\,\mathrm{mg\,m^{-2}}$; ERF: $-0.3\,\mathrm{mg\,m^{-2}}$, $\sim 20\,\%$). Eastern North America and Eurasia also show a similar contribution to SOA source due to anthropogenic emissions (ACB: $2.1\,\mathrm{mg\,m^{-2}}$, $\sim 78\,\%$; ERF: $-0.2\,\mathrm{mg\,m^{-2}}$, $\sim 72\,\%$). In both regions, non-biomass burning emissions provide a larger input to SOA source compared to biomass burning emissions, with a larger contribution in Eurasia compared to eastern North America (ACB: $1.4\,\mathrm{mg\,m^{-2}}$ vs. $0.9\,\mathrm{mg\,m^{-2}}$, $52\,\%$ vs. $32\,\%$) and even a different sign in ERF ($-0.2\,\mathrm{mg\,m^{-2}}$ vs. $+0.08\,\mathrm{mg\,m^{-2}}$,

$45\,\%$ vs. $25\,\%$). Compared to eastern North America and Eurasia, north-eastern China presents nearly a half nitrate source, while contributions to sulfate ACB due to anthropogenic emissions are about 0.5–$1\,\mathrm{W\,m^{-2}}$ (5–$10\,\%$) larger, and lead to more intense negative ERF (by 0.4–$0.6\,\mathrm{W\,m^{-2}}$, 5–$10\,\%$). In the north-eastern China, anthropogenic emissions largely contribute as well to SOA source with a share between biomass and non-biomass burning similar to Eurasia. The north-western Amazon Basin shows the smallest contributions to SA sources. However, compared to the other key regions, biomass burning and non-biomass burning emissions contribute by the same amount to SOA source (ACB: $0.5\,\mathrm{W\,m^{-2}}$, 24–$29\,\%$; ERF: $-0.06\,\mathrm{W\,m^{-2}}$, 24–$29\,\%$). As previously commented, central Africa substantially contributes to sulfate source via both biomass (ACB: $0.6\,\mathrm{W\,m^{-2}}$, $30\,\%$; ERF: $-0.2\,\mathrm{W\,m^{-2}}$, $30\,\%$) and non-biomass burning emissions (ACB: $0.7\,\mathrm{W\,m^{-2}}$, $40\,\%$; ERF: $-0.3\,\mathrm{W\,m^{-2}}$, $45\,\%$). In this region, biomass burning emissions substantially feed SOA source, with contributions that nearly double those from non-biomass burning emissions (ACB: $2.1\,\mathrm{W\,m^{-2}}$ vs. $1.1\,\mathrm{W\,m^{-2}}$, $44\,\%$ vs. $22\,\%$; ERF: $-0.16\,\mathrm{W\,m^{-2}}$ vs. $-0.08\,\mathrm{W\,m^{-2}}$, $48\,\%$ vs. $23\,\%$).

3.3 Aerosol pollution changes to surface solar radiation

3.3.1 Global-scale

The global annual average shortwave visible solar radiation (total, direct and diffuse) for each simulations (control and sensitivity) are gathered in Table 3. Hereafter, we shorten "shortwave visible solar radiation" to "radiation". Relative to the control simulation (SimCTRL), changes in global total and diffuse radiation are slightly affected by the pollution aerosol burden (absolute change for total radiation: from $+1.6\,\mathrm{W\,m^{-2}}$ to $+5.1\,\mathrm{W\,m^{-2}}$; absolute change for diffuse radiation: from $-1.3\,\mathrm{W\,m^{-2}}$ to $-3.8\,\mathrm{W\,m^{-2}}$; relative change: 1.7–$2.5\,\%$). On the contrary, changes in direct radiation shows a larger sensitivity range to the aerosol burden (absolute change: 2.9–$8.9\,\mathrm{W\,m^{-2}}$; relative change: 3.6–$11.2\,\%$). In the present-day world, anthropogenic pollution aerosols drive a decrease in global total and direct radiation by $-2.3\,\%$ ($-5.2\,\mathrm{W\,m^{-2}}$) and $-11.2\,\%$ ($-9.0\,\mathrm{W\,m^{-2}}$), respectively, while global diffuse radiation increases by $+2.5\,\%$ ($+3.7\,\mathrm{W\,m^{-2}}$). Biomass burning aerosols have almost zero effects on global total and diffuse radiation, while they reduce direct radiation by $-3.6\,\%$ ($-2.9\,\mathrm{W\,m^{-2}}$). Non-biomass burning aerosols (non-BBAs) decrease global total radiation by $-1.7\,\%$ ($-3.8\,\mathrm{W\,m^{-2}}$) and increase global diffuse radiation by the same percentage (absolute change: $+2.6\,\mathrm{W\,m^{-2}}$), while global direct radiation reduces by $-8.0\,\%$ ($-6.4\,\mathrm{W\,m^{-2}}$). In summary, anthropogenic pollution aerosols drive an overall SSR (direct+diffuse) global decline of $\sim 5\,\mathrm{W\,m^{-2}}$. In the literature, estimates for the overall SSR decline during the "global dimming" (period 1950–1980) range from 3 to $9\,\mathrm{W\,m^{-2}}$ (Wild, 2012). In percentage, anthropogenic pollution aerosols drive an overall SSR global decline of $8.7\,\%$.

3.3.2 Five key regions

Figure 4 shows the spatial distribution of aerosol-driven annual absolute changes in surface radiation (for annual percentage and seasonal absolute changes: Fig. S1 and S2 in the Supplementary Material). Regionally, on both annual and seasonal average, eastern North America, Eurasia, north-eastern China, the north-western Amazon basin and central Africa are highly affected by aerosol-induced changes in surface solar radiation. For these five key regions, Table 5 presents absolute and percent changes in annual average radiation (total, direct and diffuse) between the control and sensitivity simulations. The eastern North America shows the largest increase in annual diffuse radiation due to all anthropogenic aerosols ($+8.6\,\mathrm{W\,m^{-2}}$; $+6.2\,\%$), followed by north-eastern China and central Africa, which experience similar changes ($\sim +7.4$–$7.9\,\mathrm{W\,m^{-2}}$; $\sim +5.7\,\%$). Over the eastern North-America, the increase in diffuse radiation maximizes during boreal summer ($+13.6\,\mathrm{W\,m^{-2}}$; $+8.9\,\%$), with changes that are 1.6–$5.7\,\mathrm{W\,m^{-2}}$ (1.9–$3.3\,\%$) higher that those observed over north-eastern China and Eurasia (Table S3 in the Supplementary Material). Driven by non-BBAs, Eurasia and north-eastern China undergo the largest reduction in total and direct radiation with a larger increase over north-eastern China (total: $-12.3\,\mathrm{W\,m^{-2}}$, $-6\,\%$; direct: $-19.4\,\mathrm{W\,m^{-2}}$, $-26.1\,\%$) than Eurasia (total: $-9.5\,\mathrm{W\,m^{-2}}$, $-4.8\,\%$; direct: $-14\,\mathrm{W\,m^{-2}}$, $-23.8\,\%$). Over Eurasia and north-eastern China, decreases in total and direct radiation maximize during boreal summer, with changes that double those observed over eastern North-America (Table S3 in the Supplementary Material). In Central Africa and the north-eastern Amazon, on an annual average basis, BBAs drive changes in surface radiation that are similar in magnitude to those driven by non-BBAs. Yet, in these tropical ecosystems, the BBA effects on surface radiation exhibit a strong seasonal cycle with the maximum signal in the dry-fire season (boreal summer–boreal autumn, JJA–SON).

For these five key regions, our results are broadly consistent with Mercado et al. (2009) and Chen and Zhuang (2014), with one exception. Over the Amazon basin, Chen and Zhuang (2014) simulated an aerosol-driven decrease in diffuse radiation; the authors ascribed this behavior to the combination of an aerosol-driven decrease in total radiation (less solar radiation to be scattered above, and subsequently under, clouds) with the high cloud fractions over the Amazon basin (cloud scattering effectively limits aerosol light scattering).

3.4 Aerosol pollution changes to surface meteorology

Accounting for only the direct aerosol effect and using the fixed-SST technique, we limit the influence of pollution aerosols on the Earth System to direct changes in surface radiation that affect the atmosphere and land-surface only. For this reason, in the following we mainly relate changes in land carbon fluxes to changes in surface radiation, surface meteorology (e.g., SAT and relative humidity) and plant conditions (e.g., transpiration, canopy temperature).

The radiation changes caused by anthropogenic aerosol pollution do not exert a statistically significant change in global and annual average SAT because our experiments use fixed SSTs and do not consider aerosol indirect effects on clouds. The rapid adjustments are allowed for the atmosphere and land-surface only. For the same reasons, we do not find statistically significant changes in precipitation or in cloud water content due to anthropogenic aerosol pollution (not shown). The model does simulate statistically robust changes in annual average SAT in the two tropical key regions: the north-western Amazon Basin and central Africa (Fig. S3 in the Supplementary Material). From the sensitivity experiments, we ascertain that the SAT changes are associated with the BBAs in the tropical regions (Fig. S3 and Table S4 in the Supplementary Material). The mechanism occurs through a bio-meteorological feedback described below.

Figure 5 shows changes in annual transpiration efficiency (i.e., a proxy of canopy conductance), relative humidity and canopy temperature driven by anthropogenic pollution aerosols in the three sensitivity cases (Fig. S4 for the corresponding annual percentage changes and Fig. S5 for the seasonal absolute changes, both in the Supplementary Material). In the model, photosynthesis and stomatal conductance are coupled through the Farquhar–Ball–Berry approach. Direct radiative forcing-driven (DRF-driven) increases in photosynthesis and GPP are associated with increases in canopy conductance and relative humidity (RH) via increased transpiration. Under anthropogenic aerosol pollution, transpiration efficiency shows significant modifications in all five key regions (Fig. 5 and Table 5). The north-western Amazon Basin records the largest increase in transpiration efficiency due to BBAs ($\sim 0.51\,\%$; $\sim 5\,\%$). Among industrialized regions, the largest increases in transpiration efficiency are observed in Eurasia due to all anthropogenic aerosols ($0.16\,\%$; $\sim 5\,\%$), one-third of the increases in transpiration efficiency observed in the north-western Amazon Basin. Among the five key regions, changes in canopy temperature are statistically robust only in the north-western Amazon Basin, central Africa and north-eastern China. The north-western Amazon Basin experiences the largest decrease in canopy temperature driven by BBAs ($-0.31\,\mathrm{K}$; $-0.10\,\%$), which is $\sim 0.1\,\mathrm{K}$ larger than the decrease in canopy temperature over central Africa and north-eastern China. Due to anthropogenic pollution aerosols, central Africa and north-eastern China experience similar decrease in canopy temperature ($-0.23\,\mathrm{K}$; $-0.08\,\%$), and, compared to the north-western Amazon Basin, they undergo substantial decreases in direct radiation ($-35\,\%$ in central Africa and $-29\,\%$ in north-eastern China vs. $-8\,\%$ in the north-western Amazon Basin).

To summarize, in the model, reductions in the canopy temperature observed in the north-western Amazon Basin represents a positive feedback on plant productivity (further increases) in response to the DRF-driven increases. In industrial key regions such as eastern North America and Eurasia, changes in the quantity and quality of surface solar radiation play the main role in affecting plant photosynthesis. In north-eastern China and central Africa multiple aerosol-driven effects may combine to affect plant photosynthesis: changes in the quantity and quality of surface solar radiation (as

in eastern North America and Eurasia) and reductions in the canopy temperature (as in the north-western Amazon Basin).

3.5 Sensitivity of GPP to aerosol pollution

3.5.1 Global-scale

Changes in the global annual average GPP flux between the control and the sensitivity simulations are reported in Table 3. Global GPP shows a weak sensitivity to pollution aerosols ($\sim$ 1–2 %). Global GPP is increased by up to 2.0 % ($2.4\,\mathrm{PgC\,yr^{-1}}$) at most due to all anthropogenic aerosol pollution. Biomass burning and non-biomass burning aerosols have a comparable effect on global GPP. In contrast to Mercado et al. (2009), our model results do not suggest a substantial change in global GPP due to pollution aerosols.

3.5.2 Five key regions

Anthropogenic aerosol pollution drives regional increases in annual average plant productivity (GPP) that affect the five key regions (Fig. 6 and, for percentage changes, Fig. S6 in the Supplementary Material). The strongest increases in GPP occur in eastern North America and Eurasia ($+0.2$–$0.3\,\mathrm{gC\,m^{-2}\,day^{-1}}$; +5–8 %) (Fig. 6a and Fig. S7a). In the north-western Amazon Basin, BBAs drive similar absolute increases in GPP ($+0.2$–$0.3\,\mathrm{gC\,m^{-2}\,day^{-1}}$; +2–5 %) (Fig. 6b and Fig. S7b).

Anthropogenic aerosols drive the strongest absolute enhancement in GPP in Eurasia ($+0.62\,\mathrm{PgC\,yr^{-1}}$; ~ 5 %), followed by eastern North America, which experiences a third of the absolute increase in GPP but similar relative increases ($+0.21\,\mathrm{PgC\,yr^{-1}}$; ~ 5 %) (Table 5). In north-eastern China, anthropogenic aerosols drive the lowest enhancement in GPP, which is one tenth of the absolute increases in GPP observed in Eurasia ($+0.06\,\mathrm{PgC\,yr^{-1}}$; 1.2 %; Table 5). The north-western Amazon basin and central Africa records increases in GPP that are slightly stronger than those observed in north-eastern China ($+0.07$–$0.10\,\mathrm{PgC\,yr^{-1}}$; 1.6–2.4 %; Table 5).

In each key region, increases in GPP are governed by different aerosol types. In the industrial key regions, non-BBAs play a key role in GPP enhancement; while, in biomass burning regions (i.e., the north-western Amazon Basin and central Africa), BBAs govern GPP enhancement. In north-eastern China, BBAs do not drive any robust change in GPP; in Eurasia, BBAs drive increases in GPP that is two-third of the increases due to non-BBAs ($+0.2\,\mathrm{PgC\,yr^{-1}}$ vs. $+0.3\,\mathrm{PgC\,yr^{-1}}$; 1.5 % vs. 2.4 %) (Table 5). In eastern North-America, BBAs and non-BBAs contribute by a similar amount to GPP enhancement ($+0.1\,\mathrm{PgC\,yr^{-1}}$, ~ 2 %; Table 5). In central Africa, BBAs entirely control increases in GPP; whereas, in the north-western Amazon Basin, BBAs drive increases in GPP larger than the increase due to all anthropogenic aerosols and non-BBAs ($+0.1\,\mathrm{PgC\,yr^{-1}}$, 3.4 %; Table 5)

During boreal summer, anthropogenic aerosol pollution increases GPP in eastern North America and Eurasia by up to +5–8 %, 0.6–$0.8\,\mathrm{gC\,m^{-2}\,day^{-1}}$ (Fig. 7a and Fig. S7c in the Supplemen-

tary Material); particularly, in Eurasia aerosol pollution from non-BBAs drive the increase in GPP (Fig. 6c and Fig S7f in the Supplementary Material). Driven by BBAs in the dry-fire season, GPP increases by $+0.05$–$0.4\,\mathrm{gC\,m^{-2}\,day^{-1}}$ ($+2$–$5\,\%$) in eastern Europe (boreal evergreen and mixed forests), and by $+0.4$–$0.6\,\mathrm{gC\,m^{-2}\,day^{-1}}$ ($+5$–$8\,\%$) in the north-western Amazon basin (Fig. 7b and Fig. S7e in the Supplementary Material).

During boreal summer, Eurasia shows the largest absolute enhancement in GPP ($+1.8\,\mathrm{PgC\,yr^{-1}}$; $+6\,\%$), mainly driven by non-BBAs ($+1.1\,\mathrm{PgC\,yr^{-1}}$; $+3.4\,\%$) compared to BBAs ($+0.5\,\mathrm{PgC\,yr^{-1}}$; $+1.5\,\%$). The absolute GPP increase in eastern North America is one-third of that observed in Eurasia ($+0.5\,\mathrm{PgC\,yr^{-1}}$; $+6\,\%$) (Table S3 in the Supplementary Material). In the north-western Amazon Basin, the largest enhancement in GPP occurs during boreal autumn driven by BBAs ($+0.2\,\mathrm{PgC\,yr^{-1}}$; $+6\,\%$), when the largest decrease in canopy temperature is observed as well; on the contrary, changes in surface radiations maximize during boreal summer (Table S3 in the Supplementary Material). Likewise, in central Africa, changes in surface radiations peak during boreal summer, while the largest enhancement in GPP (and decrease in canopy temperature) occur during boreal winter (Table S4 in the Supplementary Material). The area selected to represent central Africa mostly stretches toward southern of the equator, where boreal winter corresponds to the growing season. The seasonal behavior of GPP in central Africa suggests that the bio-meteorological feedback to canopy temperature has a larger influence on plant productivity than reduction in direct radiation.

The GPP sensitivities to aerosol pollution in the five key regions presented in this work agree well with values from previous measurement-based and modeling studies (e.g., Niyogi et al., 2004; Steiner and Chameides, 2005; Knohl and Baldocchi, 2008; Matsui et al., 2008). Consistent with previous measurement-based studies, pollution aerosols have largest impacts on GPP for these PFTs with complex canopy architectures (e.g., Niyogi et al., 2004; Alton et al., 2007; Cirino et al., 2014). For instance, the five key regions are all populated by PFTs with multi-layer canopies, large canopy heights and LAIs, such as deciduous broadleaf forests, evergreen needleleaf forests, mixed forests, and tropical rainforests, which happen to be co-located with high sources of anthropogenic aerosol pollution. In the Amazon Basin, previous studies measured enhancement in $\mathrm{CO_2}$ uptake at ecosystem scale during biomass burning season; these observationally-based studies attributed the rise in $\mathrm{CO_2}$ uptake to the increase in diffuse light, although substantial changes in surface temperature and humidity were also measured (e.g., Oliveira et al., 2007; Doughty et al., 2010; Cirino et al., 2014). Using a modeling framework, Rap et al. (2015) estimated that BBAs enhance GPP by 0.7–$1.6\,\%$, for an increase in diffuse radiation 3.4–$6.8\,\%$. Their estimated GPP sensitivity for this region is lower than values presented here because Rap et al. (2015) did not account for aerosol-induced reductions in leaf temperature.

Anthropogenic aerosol pollution substantially enhances plant productivity at a regional scale. This analysis suggests that aerosol-driven enhancements in GPP result from different mechanisms that depend on region. In the model, light scattering and DRF dominates in eastern North America, reduc-

tion in direct radiation dominates in Eurasia and north-eastern China, and tropical ecosystems (i.e., the north-western Amazon Basin and central Africa) benefit from a bio-meteorological feedback to canopy temperature.

3.6 Sensitivity of isoprene emission to aerosol pollution

3.6.1 Global-scale

Changes in the global annual average isoprene emission between the control and the sensitivity simulations are reported in Table 3. Similar to GPP, global isoprene emission shows a weak sensitivity to pollution aerosols ($\sim$ 1–2 %). Global isoprene emission decreases by up to $1.7\,\%$ ($6.9\,\mathrm{PgC\,yr^{-1}}$) for SimNOant. Global isoprene emissions is sensitive to industrial emissions but not to biomass burning emissions.

3.6.2 Five key regions

Anthropogenic aerosol pollution drives a decrease in annual average isoprene emission of $-0.5\,\mathrm{mgC\,m^{-2}\,day^{-1}}$ to $-1\,\mathrm{mgC\,m^{-2}\,day^{-1}}$ ($-2\,\%$ to $-12\,\%$) over Europe and China (Fig. 8 and Fig. S7 in the Supplementary Material). Non-biomass burning sources are mainly responsible for the observed regional decrease in annual average isoprene emission. In peak growing season in the temperate and tropical zone, pollution aerosols do not affect isoprene emission (Fig. S8 in the Supplementary Material). On an annual average basis, anthropogenic aerosols mainly from non-biomass burning sources (i.e., BBAs have no robust effect) drive the largest decreases in isoprene source over north-eastern China ($-1.04\,\mathrm{TgC\,yr^{-1}}$; $-5.6\,\%$) and Eurasia ($-0.86\,\mathrm{TgC\,yr^{-1}}$; $-2.7\,\%$) (Table 5).

In response to aerosol pollution from non-biomass burning sources Europe and China show a large decrease in annual average direct radiation (-24–$26\,\%$), but a similar increase in diffuse radiation ($+3$–$5\,\%$) as eastern North America (Table 5). Hence, over Europe and China aerosol-driven reduction in direct light is not adequately sustained by an increase in diffuse radiation, which limits isoprene emission, due to the reduced light supply (reduced J_e). Thus, in Europe and China, we find that aerosol-induced reduction in direct radiation drives isoprene decreases and concomitant GPP increases. Even when photosynthesis is light-saturated (in a Rubisco-limited environment), isoprene emission continues to rise under increasing PAR (Morfopoulos et al., 2013). This divergent response has been observed at the ecosystem scale (Sharkey and Loreto, 1993). At $20^\circ\,\mathrm{C}$ and at any photon flux, the authors recorded nearly no isoprene emission; at $30^\circ\,\mathrm{C}$ isoprene emission increased with photon flux up to $1600\,\mu\mathrm{mol\,m^{-2}\,s^{-1}}$, while photosynthesis was already saturated; at $40^\circ\,\mathrm{C}$, isoprene emission maximized at $1000\,\mu\mathrm{mol\,m^{-2}\,s^{-1}}$, afterwards it decreased when the photon flux was raised to $1600\,\mu\mathrm{mol\,m^{-2}\,s^{-1}}$.

In the north-western Amazon Basin, annual average isoprene emission increases are simulated in response to BBAs ($+0.4\,\mathrm{TgC\,yr^{-1}}$; $+2.4\,\%$) (Table 5), although the area of statistical significance is

small. In this region, the influence of increases in GPP on isoprene emission over-rides the influence of the cooler canopy temperatures (Table 5).

4 Discussion and conclusions

Aerosol-induced effects on land carbon fluxes (GPP and isoprene emission) were investigated using a coupled global vegetation-chemistry-climate model. By performing sensitivity experiments, we isolated the role of pollution aerosol sources (anthropogenic, biomass burning and non-biomass burning). Our results suggest that global-scale land carbon fluxes (GPP and isoprene emission) are not sensitive to pollution aerosols, even under a robust overall SSR (direct+diffuse) global change ($\sim 9\,\%$). We found substantial but divergent sensitivities of GPP and isoprene emission to pollution aerosols at a regional scale. In eastern North America and Eurasia, anthropogenic pollution aerosols (mainly from non-biomass burning sources) enhance GPP by $+5$–$8\,\%$ on an annual average. In the north-western Amazon basin and central Africa, biomass burning aerosols increase GPP by $+2$–$5\,\%$ on an annual average ($+5$–$8\,\%$ at the peak of the dry-fire season in the north-western Amazon basin). In Eurasia and north-eastern China, anthropogenic pollution aerosols (mainly from non-biomass burning sources) drive a decrease in isoprene emission of $-2\,\%$ to $-12\,\%$ on annual average. Our model results imply that reductions of anthropogenic pollution aerosols over Europe and China below the present day loadings may trigger an enhancement in isoprene emission, with consequences for ozone and aerosol air quality.

We acknowledge three main limitations. Firstly, we tackled the direct aerosol effects only and did not consider 1st and 2nd indirect effects of aerosols such that we are partly missing the impact of aerosol-cloud interactions on land carbon fluxes. Secondly, we used the fixed SST-technique, hence we accounted only for rapid adjustments of land surface climate to aerosol radiation perturbation. Thirdly, we did not include feedbacks from dynamic LAI and phenology that may lead to an underestimation of the effects of aerosol-induced effects on plant-productivity. Future research will address these three limitations. Future changes in regional atmospheric aerosol loadings will have substantial implications for the regional land carbon cycle.

Author contributions. S. Strada and N. Unger designed the experiments. S. Strada performed the simulations. S. Strada and N. Unger prepared the manuscript.

Acknowledgements. This project was supported in part by the facilities and staff of the Yale University Faculty of Arts and Sciences High Performance Computing Center.

References

Alton, P. B., North, P. R., and Los, S. O.: The impact of diffuse sunlight on canopy light-use efficiency, gross photosynthetic product and net ecosystem exchange in three forest biomes, Global Change Biol., 13, 776–787, 2007.

Arneth, A., Monson, R. K., Schurgers, G., Niinemets, Ü., and Palmer, P. I.: Why are estimates of global terrestrial isoprene emissions so similar (and why is this not so for monoterpenes)?, Atmos. Chem. Phys., 8, 4605–4620, doi:10.5194/acp-8-4605-2008, 2008.

Arneth, A., Schurgers, G., Lathiere, J., Duhl, T., Beerling, D. J., Hewitt, C. N., Martin, M., and Guenther, A.: Global terrestrial isoprene emission models: sensitivity to variability in climate and vegetation, Atmos. Chem. Phys., 11, 8037–8052, doi:10.5194/acp-11-8037-2011, 2011.

Artaxo, P., Rizzo, L. V., Brito, J. F., Barbosa, H. M. J., Arana, A., Sena, E. T., Cirino, G. G., Bastos, W., Martin, S. T., and Andreae, M. O.: Atmospheric aerosols in Amazonia and land use change: from natural biogenic to biomass burning conditions, Faraday Discuss., 165, 203–235, doi:10.1039/C3FD00052D, 2013.

Ball, J. T., Woodrow, I. E., and Berry, J. A.: A model predicting stomatal conductance and its contribution to the control of photosynthesis under different environmental conditions. In: Progress in Photosynthesis Research, Biggins, J. (Ed.), Nijhoff, Dordrecht, Netherlands, 221-224, 1987

Bauer, S. E., Koch, D., Unger, N., Metzger, S. M., Shindell, D. T., and Streets, D. G.: Nitrate aerosols today and in 2030: a global simulation including aerosols and tropospheric ozone, Atmos. Chem. Phys., 7, 5043–5059, doi:10.5194/acp-7-5043-2007, 2007.

Beer, C., Reichstein, M., Tomelleri, E., Ciais, P., Jung, M., Carvalhais, N., Rödenbeck, C., Arain, M. A., Baldocchi, D., Bonan, G. B., Bondeau, A., Cescatti, A., Lasslop, G., Lindroth, A., Lomas, M., Luyssaert, S., Margolis, H., Oleson, K. W., Roupsard, O., Veenendaal, E., Viovy, N., Williams, C., Woodward, F. I., and Papale, D.: Terrestrial gross carbon dioxide uptake: global distribution and covariation with climate, Science, 329, 834–838, 2010.

Bell, N., Koch, D., and Shindell, D.: Impacts of chemistry-aerosol coupling on tropospheric ozone and sulfate simulations in a general circulation model, J. Geophys. Res.-Atmos., 110, D14, doi:10.1029/2004JD005538, 2005.

Bian, H., Chin, M., Kawa, S. R., Yu, H., Diehl, T., and Kucsera, T.: Multiscale carbon monoxide and aerosol correlations from satellite measurements and the GOCART model: implication for emissions and atmospheric evolution, J. Geophys. Res.-Atmos., 115, D07302, doi:10.1029/2009JD012781, 2010.

Bonan, G. B., Lawrence, P. J., Oleson, K. W., Levis, S., Jung, M., Reichstein, M., Lawrence, D., and Swenson, S. C.: Improving canopy processes in the Community Land Model version 4 (CLM4) using global flux fields empirically inferred from FLUXNET data, J. Geophys. Res.-Biogeo., 116, G2, doi:10.1029/2010JG001593, 2011.

Boucher, O., Randall, D., Artaxo, P., Bretherton, C., Feingold, G., Forster, P., Kerminen, V.-M., Kondo, Y., Liao, H., Lohmann, U., Rasch, P., Satheesh, S. K., Sherwood, S., Stevens, B., and Zhang, X. Y.: Clouds and Aerosols, in: Climate Change 2013: The Physical Science Basis. Contribution of Working Group I to the Fifth Assessment Report of the Intergovernmental Panel on Climate Change, Cambridge University Press, Cambridge, UK and New York, NY, USA, 571–656, 2013.

Carlton, A. G., Pinder, R. W., Bhave, P. V., and Pouliot, G. A.: To what extent can biogenic SOA be controlled?, Environ. Sci. Technol., 44, 3376–3380, 2010.

Chen, M. and Zhuang, Q.: Evaluating aerosol direct radiative effects on global terrestrial ecosystem carbon dynamics from 2003 to 2010, Tellus B, 66, 21808, doi:10.3402/tellusb.v66.21808, 2014.

Cheng, S. J., Bohrer, G., Steiner, A. L., Hollinger, D. Y., Suyker, A., Phillips, P. R., and Nadelhoffer, K. J.: Variations in the influence of diffuse light on gross primary productivity in temperate ecosystems, Agr. Forest Meteorol., 201, 98–110, 2015.

Cirino, G. G., Souza, R. A. F., Adams, D. K., and Artaxo, P.: The effect of atmospheric aerosol particles and clouds on net ecosystem exchange in the Amazon, Atmos. Chem. Phys., 14, 6523–6543, doi:10.5194/acp-14-6523-2014, 2014.

Doughty, C. E., Flanner, M. G., and Goulden, M. L.: Effect of smoke on subcanopy shaded light, canopy temperature, and carbon dioxide uptake in an Amazon rainforest, Global Biogeochem. Cy., 24, GB3015, doi:10.1029/2009GB003670, 2010.

Farquhar, G. D., von Caemmerer, S. V., and Berry, J. A.: A biochemical model of photosynthetic CO_2 assimilation in leaves of C_3 species, Planta, 149, 78–90, 1980.

Ford, B. and Heald, C. L.: Aerosol loading in the Southeastern United States: reconciling surface and satellite observations, Atmos. Chem. Phys., 13, 9269–9283, doi:10.5194/acp-13-9269-2013, 2013.

Forster, P., Ramaswamy, V., Artaxo, P., Berntsen, T., Betts, R., Fahey, D. W., Haywood, J., Lean, J., Lowe, D. C., Myhre, G., Nganga, J., Prinn, R., Raga, G., Schulz, M. and Van Dorland, R.: Changes in Atmospheric Constituents and in Radiative Forcing, in: Climate Change 2007: The Physical Science Basis. Contribution of Working Group I to the Fourth Assessment Report of the Intergovernmental Panel on Climate Change, Cambridge University Press, Cambridge, UK and New York, NY, USA, 2007.

Friend, A. D. and Kiang, N. Y.: Land surface model development for the GISS GCM: effects of improved canopy physiology on simulated climate, J. Climate, 18, 2883–2902, 2005.

Gu, L., Baldocchi, D., Verma, S. B., Black, T., Vesala, T., Falge, E. M., and Dowty, P. R.: Advantages of diffuse radiation for terrestrial ecosystem productivity, J. Geophys. Res.-Atmos., 107, D6, doi:10.1029/2001JD001242, 2002.

Gu, L., Baldocchi, D. D., Wofsy, S. C., Munger, J. W., Michalsky, J. J., Urbanski, S. P., and Boden, T. A.: Response of a deciduous forest to the Mount Pinatubo eruption: enhanced photosynthesis, Science, 299, 2035–2038, 2003.

Guenther, A., Karl, T., Harley, P., Wiedinmyer, C., Palmer, P. I., and Geron, C.: Estimates of global terrestrial isoprene emissions using MEGAN (Model of Emissions of Gases and Aerosols from Nature), Atmos. Chem. Phys., 6, 3181–3210, doi:10.5194/acp-6-3181-2006, 2006.

Hsu, N. C., Tsay, S.-C., King, M., and Herman, J. R.: Aerosol properties over bright-reflecting source regions, IEEE T. Geosci. Remote, 42, 557–569, doi:10.5194/amt-7-1791-2014, 2004.

Jones, C. D. and Cox, P. M.: Modeling the volcanic signal in the atmospheric CO_2 record, Global Biogeochem. Cy., 15, 453–465, 2001.

Jung, M., Reichstein, M., Margolis, H. A., Cescatti, A., Richardson, A. D., Arain, M. A., Arneth, A., Bernhofer, C., Bonal, D., Chen, J., Gianelle, D., Gobron, N., Kiely, G., Kutsch, W., Lasslop, G., Law, B. E., Lindroth, A., Merbold, L., Montagnani, L., Moors, E. J., Papale, D., Sottocornola, M., Vaccari, F., and

Williams, C.: Global patterns of land-atmosphere fluxes of carbon dioxide, latent heat, and sensible heat derived from eddy covariance, satellite, and meteorological observations, J. Geophys. Res.-Biogeo., 116, G3, doi:10.1029/2010JG001566, 2011.

Kanniah, K. D., Beringer, J., North, P., and Hutley, L.: Control of atmospheric particles on diffuse radiation and terrestrial plant productivity: a review, Prog. Phys. Geogr., 36, 209–237, 2012.

Keeling, C. D., Whorf, T. P., Wahlen, M., and Plicht, J. V. D.: Interannual extremes in the rate of rise of atmospheric carbon dioxide since 1980, Nature, 375, 666–670, 1995.

Knohl, A. and Baldocchi, D. D.: Effects of diffuse radiation on canopy gas exchange processes in a forest ecosystem, J. Geophys. Res.-Biogeo., 113, G2, doi:10.1029/2007JG000663, 2008.

Koch, D. and Del Genio, A. D.: Black carbon semi-direct effects on cloud cover: review and synthesis, Atmos. Chem. Phys., 10, 7685–7696, doi:10.5194/acp-10-7685-2010, 2010.

Koch, D. and Hansen, J.: Distant origins of Arctic black carbon: a Goddard Institute for Space Studies ModelE experiment, J. Geophys. Res., 110, 7685–7696, doi:10.1029/2004JD005296, 2005.

Koch, D., Schmidt, G. A., and Field, C. V.: Sulfur, sea salt, and radionuclide aerosols in GISS ModelE, J. Geophys. Res., 111, doi:10.1029/2004JD005550, 2006.

Koch, D., Menon, S., Del Genio, A., Ruedy, R., Alienov, I., and Schmidt, G. A.: Distinguishing aerosol impacts on climate over the past century, J. Climate, 22, 2659–2677, doi:10.1175/2008JCLI2573.1, 2009.

Laffineur, Q., Aubinet, M., Schoon, N., Amelynck, C., Müller, J.-F., Dewulf, J., Steppe, K., and Heinesch, B.: Impact of diffuse light on isoprene and monoterpene emissions from a mixed temperate forest, Atmos. Environ., 74, 385–392, 2013.

Lamarque, J.-F., Bond, T. C., Eyring, V., Granier, C., Heil, A., Klimont, Z., Lee, D., Liousse, C., Mieville, A., Owen, B., Schultz, M. G., Shindell, D., Smith, S. J., Stehfest, E., Van Aardenne, J., Cooper, O. R., Kainuma, M., Mahowald, N., McConnell, J. R., Naik, V., Riahi, K., and van Vuuren, D. P.: Historical (1850–2000) gridded anthropogenic and biomass burning emissions of reactive gases and aerosols: methodology and application, Atmos. Chem. Phys., 10, 7017–7039, doi:10.5194/acp-10-7017-2010, 2010.

Levy, R. C., Remer, L. A., Kleidman, R. G., Mattoo, S., Ichoku, C., Kahn, R., and Eck, T. F.: Global evaluation of the Collection 5 MODIS dark-target aerosol products over land, Atmos. Chem. Phys., 10, 10399–10420, doi:10.5194/acp-10-10399-2010, 2010.

Matsui, T., Beltrán-Przekurat, A., Niyogi, D., Pielke, R. A., and Coughenour, M.: Aerosol light scattering effect on terrestrial plant productivity and energy fluxes over the eastern United States, J. Geophys. Res.-Atmos., 113, D14, doi:10.1029/2007JD009658, 2008.

Mercado, L. M., Bellouin, N., Sitch, S., Boucher, O., Huntingford, C., Wild, M., and Cox, P. M.: Impact of changes in diffuse radiation on the global land carbon sink, Nature, 458, 1014–1017, 2009.

Messina, P., Lathière, J., Sindelarova, K., Vuichard, N., Granier, C., Ghattas, J., Cozic, A., and Hauglustaine, D. A.: Global biogenic volatile organic compound emissions in the ORCHIDEE and MEGAN models and sensitivity to key parameters, Atmos. Chem. Phys. Discuss., 15, 33967–34033, doi:10.5194/acpd-15-33967-2015, 2015.

Miller, R., Cakmur, R. V., Perlwitz, J. P., Geogdzhayev, I. V., Ginoux, P., Kohfeld, K. E., Koch, D., Prigent, C., Ruedy, R., Schmidt, G. A., and Tegen, I.: Mineral dust aerosols in the NASA Goddard Insti-

tute for Space Sciences ModelE atmospheric general circulation model, J. Geophys. Res., 111, 474–487, doi:10.1029/2005JD005796, 2006.

Molineaux, B. and Ineichen, P.: Impact of Pinatubo aerosols on the seasonal trends of global, direct and diffuse irradiance in two northern mid-latitude sites, Sol. Energy, 58, 91–101, doi:10.1016/0038-092X(96)00051-5, 1996.

Morfopoulos, C., Prentice, I. C., Keenan, T. F., Friedlingstein, P., Medlyn, B. E., Peñuelas, J., and Possell, M.: A unifying conceptual model for the environmental responses of isoprene emissions from plants, Ann. Bot.-London, 112, 1223–1238, doi:10.1093/aob/mct206, 2013.

Myhre, G., Samset, B. H., Schulz, M., Balkanski, Y., Bauer, S., Berntsen, T. K., Bian, H., Bellouin, N., Chin, M., Diehl, T., Easter, R. C., Feichter, J., Ghan, S. J., Hauglustaine, D., Iversen, T., Kinne, S., Kirkevåg, A., Lamarque, J.-F., Lin, G., Liu, X., Lund, M. T., Luo, G., Ma, X., van Noije, T., Penner, J. E., Rasch, P. J., Ruiz, A., Seland, Ø., Skeie, R. B., Stier, P., Takemura, T., Tsigaridis, K., Wang, P., Wang, Z., Xu, L., Yu, H., Yu, F., Yoon, J.-H., Zhang, K., Zhang, H., and Zhou, C.: Radiative forcing of the direct aerosol effect from AeroCom Phase II simulations, Atmos. Chem. Phys., 13, 1853–1877, doi:10.5194/acp-13-1853-2013, 2013a.

Myhre, G., Shindell, D., Bréon, F.-M., Collins, W., Fuglestvedt, J., Huang, J., Koch, D., Lamarque, J.-F., Lee, D., Mendoza, B., Nakajima, T., Robock, A., Stephens, G., Takemura, T., and Zhang, H.: Anthropogenic and natural radiative forcing, in: Climate Change 2013: The Physical Science Basis. Contribution of Working Group I to the Fifth Assessment Report of the Intergovernmental Panel on Climate Change, Cambridge University Press, Cambridge, UK and New York, NY, USA, 659–740, doi:10.1017/CBO9781107415324.018, 2013b.

Niyogi, D., Chang, H.-I., Saxena, V. K., Holt, T., Alapaty, K., Booker, F., Chen, F., Davis, K. J., Holben, B., Matsui, T., Meyers, T., Oechel, W. C., Pielke, R. A., Wells, R., Wilson, K., and Xue, Y.: Direct observations of the effects of aerosol loading on net ecosystem CO_2 exchanges over different landscapes, Geophys. Res Lett., 31, 20, doi:10.1029/2004GL020915, 2004.

Oliveira, P. H. F., Artaxo, P., Pires, C., De Lucca, S., Procópio, A., Holben, B., Schafer, J., Cardoso, L. F., Wofsy, S. C., and Rocha, H. R.: The effects of biomass burning aerosols and clouds on the CO_2 flux in Amazonia, Tellus B, 59, 338–349, 2007.

Pacifico, F., Harrison, S. P., Jones, C. D., and Sitch, S.: Isoprene emissions and climate, Atmos. Environ., 43, 6121–6135, doi:10.1016/j.atmosenv.2009.09.002, 2009.

Ramanathan, V., Crutzen, P., Kiehl, J., and Rosenfeld, D.: Aerosols, climate, and the hydrological cycle, Science, 294, 2119–2124, 2001.

Rap, A., Spracklen, D. V., Mercado, L., Reddington, C. L., Haywood, J. M., Ellis, R. J., Phillips, O. L., Artaxo, P., Bonal, D., Coupe, N. R., and Butt, N.: Fires increase Amazon forest productivity through increases in diffuse radiation, Geophys. Res. Lett., 42, 4654–4662, doi:10.1002/2015GL063719, 2015.

Rayner, N., Brohan, P., Parker, D., Folland, C., Kennedy, J., Vanicek, M., Ansell, T., and Tett, S.: Improved analyses of changes and uncertainties in sea surface temperature measured in situ since the mid-nineteenth century: the HadSST2 dataset, J. Climate, 19, 446–469, 2006.

Rosenfeld, D., Lohmann, U., Raga, G. B., O'Dowd, C. D., Kulmala, M., Fuzzi, S., Reissell, A., and Andreae, M. O.: Flood or drought: how do aerosols affect precipitation?, Science, 321, 1309–1313, 2008.

Rosenzweig, C. and Abramopoulos, F.: Land-surface model development for the GISS GCM, J. Climate, 10, 2040–2054, doi:10.1175/1520-0442(1997)010<2040:LSMDFT>2.0.CO;2, 1997.

Schmidt, G. A., Ruedy, R., Hansen, J. E., Aleinov, I., Bell, N., Bauer, M., Bauer, S., Cairns, B., Canuto, V., Cheng, Y., Del Genio, A., Faluvegi, G., Friend, A. D., Hall, T. M., Hu, Y., Kelley, M., Kiang, N. Y., Koch, D., Lacis, A. A., Lerner, J., Lo, K. K., Miller, R. L., Nazarenko, L., Oinas, V., Perlwitz, J. P., Perlwitz, J., Rind, D., Romanou, A., Russell, G. L., Sato, M., Shindell, D. T., Stone, P. H., Sun, S., Tausnev, N., Thresher, D., and Yao, M.-S.: Present-day atmospheric simulations using GISS ModelE: comparison to in situ, satellite, and reanalysis data, J. Climate, 19, 153–192, 2006.

Schmidt, G. A., Kelley, M., Nazarenko, L., Ruedy, R., Russell, G. L., Aleinov, I., Bauer, M., Bauer, S. E., Bhat, M. K., Bleck, R., Canuto, V., Chen, Y.-H., Cheng, Y., Clune, T. L., Del Genio, A., de Fainchtein, R., Faluvegi, G., Hansen, J. E., Healy, R. J., Kiang, N. Y., Koch, D., Lacis, A. A., LeGrande, A. N., Lerner, J., Lo, K. K., Matthews, E. E., Menon, S., Miller, R. L., Oinas, V., Oloso, A. O., Perlwitz, J. P., Puma, M. J., Putman, W. M., Rind, D., Romanou, A., Sato, M., Shindell, D. T., Sun, S., Syed, R. A., Tausnev, N., Tsigaridis, K., Unger, N., Voulgarakis, A., Yao, M.-S., and Zhangand, J.: Configuration and assessment of the GISS ModelE2 contributions to the CMIP5 archive, J. Adv. Model. Earth Syst., 6, 141–184, doi:10.1002/2013MS000265, 2014.

Sharkey, T. D. and Loreto, F.: Water stress, temperature, and light effects on the capacity for isoprene emission and photosynthesis of kudzu leaves, Oecologia, 95, 328–333, 1993.

Shi, Y., Zhang, J., Reid, J. S., Liu, B., and Hyer, E. J.: Critical evaluation of cloud contamination in the MISR aerosol products using MODIS cloud mask products, Atmos. Meas. Tech., 7, 1791–1801, doi:10.5194/amt-7-1791-2014, 2014.

Shindell, D. T., Faluvegi, G., Unger, N., Aguilar, E., Schmidt, G. A., Koch, D. M., Bauer, S. E., and Miller, R. L.: Simulations of preindustrial, present-day, and 2100 conditions in the NASA GISS composition and climate model G-PUCCINI, Atmos. Chem. Phys., 6, 4427–4459, doi:10.5194/acp-6-4427-2006, 2006.

Shindell, D. T., Pechony, O., Voulgarakis, A., Faluvegi, G., Nazarenko, L., Lamarque, J.-F., Bowman, K., Milly, G., Kovari, B., Ruedy, R., and Schmidt, G. A.: Interactive ozone and methane chemistry in GISS-E2 historical and future climate simulations, Atmos. Chem. Phys., 13, 2653–2689, doi:10.5194/acp-13-2653-2013, 2013a.

Shindell, D. T., Lamarque, J.-F., Schulz, M., Flanner, M., Jiao, C., Chin, M., Young, P. J., Lee, Y. H., Rotstayn, L., Mahowald, N., Milly, G., Faluvegi, G., Balkanski, Y., Collins, W. J., Conley, A. J., Dalsoren, S., Easter, R., Ghan, S., Horowitz, L., Liu, X., Myhre, G., Nagashima, T., Naik, V., Rumbold, S. T., Skeie, R., Sudo, K., Szopa, S., Takemura, T., Voulgarakis, A., Yoon, J.-H., and Lo, F.: Radiative forcing in the ACCMIP historical and future climate simulations, Atmos. Chem. Phys., 13, 2939–2974, doi:10.5194/acp-13-2939-2013, 2013b.

Spitters, C. J. T., Toussaint, H. A. J. M., and Goudriaan, J.: Separating the diffuse and direct component of global radiation and its implications for modeling canopy photosynthesis Part I. Components of incoming radiation, Agr. Forest Meteorol., 38, 217–229, 1986.

Stavrakou, T., Müller, J.-F., Bauwens, M., De Smedt, I., Van Roozendael, M., Guenther, A., Wild, M., and Xia, X.: Isoprene emissions over Asia 1979–2012: impact of climate and land-use changes, Atmos. Chem. Phys., 14, 4587–4605, doi:10.5194/acp-14-4587-2014, 2014.

Steiner, A. L. and Chameides, W. L.: Aerosol-induced thermal effects increase modelled terrestrial photosynthesis and transpiration, Tellus B, 57, 404–411, 2005.

Stevenson, D. S., Young, P. J., Naik, V., Lamarque, J.-F., Shindell, D. T., Voulgarakis, A., Skeie, R. B., Dalsoren, S. B., Myhre, G., Berntsen, T. K., Folberth, G. A., Rumbold, S. T., Collins, W. J., MacKenzie, I. A., Doherty, R. M., Zeng, G., van Noije, T. P. C., Strunk, A., Bergmann, D., Cameron-Smith, P., Plummer, D. A., Strode, S. A., Horowitz, L., Lee, Y. H., Szopa, S., Sudo, K., Nagashima, T., Josse, B., Cionni, I., Righi, M., Eyring, V., Conley, A., Bowman, K. W., Wild, O., and Archibald, A.: Tropospheric ozone changes, radiative forcing and attribution to emissions in the Atmospheric Chemistry and Climate Model Intercomparison Project (ACCMIP), Atmos. Chem. Phys., 13, 3063–3085, doi:10.5194/acp-13-3063-2013, 2013.

Streets, D. G., Yan, F., Chin, M., Diehl, T., Mahowald, N., Schultz, M., Wild, M., Wu, Y., and Yu, C.: Anthropogenic and natural contributions to regional trends in aerosol optical depth, 1980–2006, J. Geophys. Res.-Atmos., 114, D10, doi:10.1029/2008JD011624, 2009.

Trenberth, K. E. and Dai, A.: Effects of Mount Pinatubo volcanic eruption on the hydrological cycle as an analog of geoengineering, Geophys. Res. Lett., 34, L15702, doi:10.1029/2007GL030524, 2007.

Tsigaridis, K. and Kanakidou, M.: Secondary organic aerosol importance in the future atmosphere, Atmos. Environ., 41, 4682–4692, 2007.

Unger, N.: Global climate impact of civil aviation for standard and desulfurized jet fuel, Geophys. Res. Lett., 38, 20, doi:10.1029/2011GL049289, 2011.

Unger, N., Harper, K., Zheng, Y., Kiang, N. Y., Aleinov, I., Arneth, A., Schurgers, G., Amelynck, C., Goldstein, A., Guenther, A., Heinesch, B., Hewitt, C. N., Karl, T., Laffineur, Q., Langford, B., McKinney, K. A., Misztal, P., Potosnak, M., Rinne, J., Pressley, S., Schoon, N., and Serça, D.: Photosynthesis-dependent isoprene emission from leaf to planet in a global carbon–chemistry–climate model, Atmos. Chem. Phys., 13, 10243–10269, doi:10.5194/acp-13-10243-2013, 2013.

Von Caemmerer, S. V. and Farquhar, G. D.: Some relationships between the biochemistry of photosynthesis and the gas exchange of leaves, Planta, 153, 376–387, 1981.

Wild, M.: Global dimming and brightening: a review, J. Geophys. Res.-Atmos., 114, D10, doi:10.1029/2008JD011470, 2009.

Wild, M.: Enlightening global dimming and brightening, B. Am. Meteorol. Soc., 93, 27–37, 2012.

Wild, M., Trüssel, B., Ohmura, A., Long, C. N., König-Langlo, G., Dutton, E. G., and Tsvetkov, A.: Global dimming and brightening: an update beyond 2000, J. Geophys. Res.-Atmos., 114, D10, doi:10.1029/2008JD011382, 2009.

Yuan, W., Liu, S., Yu, G., Bonnefond, J.-M., Chen, J., Davis, K., Desai, A. R., Goldstein, A. H., Gianelle, D., Rossi, F., Suyker, A. E., and Verma, S. B.: Global estimates of evapotranspiration and gross primary production based on MODIS and global meteorology data, Remote Sens. Environ., 114, 1416–1431, 2010.

Yue, X. and Unger, N.: The Yale Interactive terrestrial Biosphere model version 1.0: description, evaluation and implementation into NASA GISS ModelE2, Geosci. Model Dev., 8, 2399–2417, doi:10.5194/gmd-8-2399-2015, 2015.

Yue, X., Unger, N., Keenan, T. F., Zhang, X., and Vogel, C. S.: Probing the past 30-year phenology trend of US deciduous forests, Biogeosciences, 12, 4693-4709, doi:10.5194/bg-12-4693-2015, 2015.

Yue, X., Unger, N., and Zheng, Y.: Distinguishing the drivers of trends in land carbon fluxes and plant volatile emissions over the past 3 decades, Atmos. Chem. Phys., 15, 11931-11948, doi:10.5194/acp-15-11931-2015, 2015.

Table 1. Global annual average of aerosol column burden (ACB, $\mathrm{mg\,m^{-2}}$) as simulated by NASA ModelE2-YIBs in the control and sensitivity present-day simulations for, in the order: sulfates, nitrates, organic (OC) and black carbon (BC) from industrial (ind) and biomass burning (bb), and secondary organic aerosols (SOA). Cases filled with "–" refer to negligible values of ACB (i.e., order of magnitude: $\mathrm{pg\,m^{-2}}$). For sensitivity simulations, percentage values in parentheses indicate contribution of target emissions (i.e., anthropogenic, biomass burning and non-biomass burning) to each aerosol component.

Simulation	ACB ($\mathrm{mg\,m^{-2}}$)						
	SO_4	NO_3	OC_{ind}	OC_{bb}	BC_{ind}	BC_{bb}	SOA
SimCTRL	2.41	5.16	0.48	0.97	0.17	0.09	1.37
SimNOant	1.55 (35.68 %)	0.69 (86.63 %)	–	–	–	–	0.39 (71.53 %)
SimNObb	2.42	3.54 (31.40 %)	0.48	–	0.17	–	1.14 (16.79 %)
SimNOind	1.51 (37.34 %)	1.47 (71.51 %)	–	0.82 (15.46 %)		0.08 (11.11 %)	0.90 (34.31 %)

Table 2. Global annual average of effective radiative forcing (ERF) for aerosol–radiation interactions ($\mathrm{W\,m^{-2}}$) as simulated by NASA ModelE2-YIBs in present-day simulations for, in the order: sulfates, nitrates, organic (OC) and black carbon (BC) from industrial (ind) and biomass burning (bb), and secondary organic aerosols (SOA). Global annual average ERF is calculated as the difference between the control experiment (SimCTRL) and sensitivity experiments: SimNOant, without all anthropogenic emissions; SimNObb, without biomass burning emissions; and SimNOind, without anthropogenic emissions except biomass burning. Percentage values in parentheses specify the contribution of target emissions (i.e., anthropogenic, biomass burning and non-biomass burning) to the ERF of selected aerosol component. The acronym "ns" indicates differences that are not statistically significant at the 95 % confidence level (based on a Student's t-test).

Species	ERF ($\mathrm{W\,m^{-2}}$)		
	SimCTRL − SimNOant	SimCTRL − SimNObb	SimCTRL − SimNOind
SO_4	−0.31 (40.17 %)	ns	−0.30 (39.75 %)
NO_3	−0.38 (85.09 %)	−0.14 (30.38 %)	−0.31 (69.80 %)
OC_{ind}	−0.06 (100.00 %)	ns	−0.06 (100.00 %)
OC_{bb}	−0.11 (100.00 %)	−0.11 (100.00 %)	−0.01 (9.43 %)
BC_{ind}	0.18 (100.00 %)	ns	0.18 (100.00 %)
BC_{bb}	0.12 (100.00 %)	0.12 (100.00 %)	0.02 (11.42 %)
SOA	0.10 (63.48 %)	−0.03 (15.86 %)	−0.05 (29.27 %)

Zhao, M., Heinsch, F. A., Nemani, R. R., and Running, S. W.: Improvements of the MODIS terrestrial gross and net primary production global data set, Remote Sens. Environ., 95, 164–176, 2005.

Zheng, Y., Unger, N., Barkley, M. P., and Yue, X.: Relationships between photosynthesis and formaldehyde as a probe of isoprene emission, Atmos. Chem. Phys., 15, 8559–8576, doi:10.5194/acp-15-8559-2015, 2015.

Table 3. Global annual average gross primary productivity (GPP), isoprene emission and shortwave visible (SW VIS) total, direct and diffuse solar radiation as simulated by NASA ModelE2-YIBs in the control and sensitivity present-day simulations. For sensitivity simulations, percentage changes compared to the control simulation are indicated in parentheses and reported only if changes are statistically significant at the 95 % confidence level.

Simulation	GPP	Isoprene	SW VIS Solar Radiation		
			Total	Direct	Diffuse
	($\mathrm{Pg\,C\,yr^{-1}}$)	($\mathrm{Tg\,C\,yr^{-1}}$)	($\mathrm{W\,m^{-2}}$)		
SimCTRL	116.0	402.8	230.9	80.3	150.6
SimNOant	113.6 ($-2.1\,\%$)	409.7 ($+1.7\,\%$)	236.1 ($+2.3\,\%$)	89.3 ($+11.2\,\%$)	146.8 ($-2.5\,\%$)
SimNObb	114.8 ($-1.0\,\%$)	402.9	232.6 ($+0.8\,\%$)	83.2 ($+3.6\,\%$)	149.4 ($-0.8\,\%$)
SimNOind	114.7 ($-1.1\,\%$)	407.8 ($+1.2\,\%$)	234.7 ($+1.7\,\%$)	86.7 ($+8.0\,\%$)	148.0 ($-1.7\,\%$)

Table 4. Linear correlation Pearson's coefficient (Pearson's R), Pearson's R squared (R^2) and root-mean-squared error (RMSE) as computed for model evaluation for annual and seasonal average coarse aerosol optical depth (AOD) and gross primary productivity (GPP). Performances of the NASA ModelE2-YIBs in the control present-day simulation ($\sim$ 2000s) are compared to: (1) MODIS AOD (at 550 nm; averaged over 2000–2007) for NASA ModelE2-YIBs $\mathrm{PM_{10}}$ optical depth, and (2) global FLUXNET-derived GPP product (averaged over 2000–2011). Only boreal summer (JJA) and winter (DJF) seasonal averages are reported.

Variable	Average	Pearson's R	R^2	$RMSE$
AOD	Annual	0.679	0.461	0.054
	JJA	0.769	0.591	0.064
	DJF	0.591	0.349	0.065
GPP	Annual	0.863	0.745	1.025
	JJA	0.782	0.611	1.796
	DJF	0.899	0.808	1.137

Table 5. Absolute and percent changes in annual average shortwave visible (SW VIS) solar radiation, surface atmospheric temperature (SAT), transpiration efficieny, canopy temperature, gross primary productivity (GPP) and isoprene emission in: eastern North America, Eurasia, north-eastern China, north-western Amazon Basin and central Africa (green boxes on Fig. 4(a)). Changes are computed between the control experiment (SimCTRL) and sensitivity experiments: SimNOant, without all anthropogenic emissions; SimNObb, without biomass burning emissions; and SimNOind, without anthropogenic emissions except biomass burning. The acronym "ns" indicates differences that are not statistically significant at the 95 % confidence level (based on a Student's t-test).

Region	Variable		SimCTRL − SimNOant	SimCTRL − SimNObb	SimCTRL − SimNOind
Eastern	SW VIS Solar Radiation	Total	$-12.16\,\mathrm{W\,m^{-2}}$	$-2.81\,\mathrm{W\,m^{-2}}$	$-7.85\,\mathrm{W\,m^{-2}}$
North America			−5.68 %	−1.31 %	−3.66 %
(70°–100° W; 36°–52° N)		Direct	$-20.76\,\mathrm{W\,m^{-2}}$	$-3.53\,\mathrm{W\,m^{-2}}$	$-12.95\,\mathrm{W\,m^{-2}}$
			−27.73 %	−4.71 %	−17.30 %
		Diffuse	$8.60\,\mathrm{W\,m^{-2}}$	ns	$5.10\,\mathrm{W\,m^{-2}}$
			6.17 %	ns	3.65 %
	SAT		ns	ns	ns
			ns	ns	ns
	Transpiration Efficiency		0.12 %	ns	ns
			3.72 %	ns	ns
	Canopy Temperature		ns	ns	ns
			ns	ns	ns
	GPP		$0.21\,\mathrm{Pg\,C\,yr^{-1}}$	$0.09\,\mathrm{Pg\,C\,yr^{-1}}$	$0.10\,\mathrm{Pg\,C\,yr^{-1}}$
			4.96 %	2.17 %	2.45 %
	Isoprene		$-0.28\,\mathrm{Tg\,C\,yr^{-1}}$	ns	ns
			−1.91 %	ns	ns
Eurasia	SW VIS Solar Radiation	Total	$-11.08\,\mathrm{W\,m^{-2}}$	$-1.67\,\mathrm{W\,m^{-2}}$	$-9.46\,\mathrm{W\,m^{-2}}$
(−10° W–80° E; 40°–65° N)			−5.59 %	−0.84 %	−4.77 %
		Direct	$-16.88\,\mathrm{W\,m^{-2}}$	$-2.33\,\mathrm{W\,m^{-2}}$	$-13.95\,\mathrm{W\,m^{-2}}$
			−28.78 %	−3.97 %	−23.79 %
		Diffuse	$5.80\,\mathrm{W\,m^{-2}}$	$0.67\,\mathrm{W\,m^{-2}}$	$4.49\,\mathrm{W\,m^{-2}}$
			4.15 %	0.48 %	3.22 %
	SAT		ns	ns	ns
			ns	ns	ns
	Transpiration Efficiency		0.16 %	ns	0.10 %
			5.09 %	ns	3.27 %
	Canopy Temperature		ns	ns	ns
			ns	ns	ns
	GPP		$0.63\,\mathrm{Pg\,C\,yr^{-1}}$	$0.19\,\mathrm{Pg\,C\,yr^{-1}}$	$0.31\,\mathrm{Pg\,C\,yr^{-1}}$
			4.85 %	1.47 %	2.41 %
	Isoprene		$-0.86\,\mathrm{Tg\,C\,yr^{-1}}$	ns	$-0.13\,\mathrm{Tg\,C\,yr^{-1}}$
			−2.71 %	ns	−3.92 %

Table 5. Continued.

Region	Variable		SimCTRL − SimNOant	SimCTRL − SimNObb	SimCTRL − SimNOind
North-eastern China	SW VIS Solar Radiation	Total	$-13.56\,\mathrm{W\,m^{-2}}$	ns	$-12.59\,\mathrm{W\,m^{-2}}$
(100°–120°E; 10°–35°N)			−6.41 %	ns	−5.95 %
		Direct	$-21.45\,\mathrm{W\,m^{-2}}$	$-2.35\,\mathrm{W\,m^{-2}}$	$-19.42\,\mathrm{W\,m^{-2}}$
			−28.87 %	−3.16 %	−26.14 %
		Diffuse	$7.89\,\mathrm{W\,m^{-2}}$	$1.08\,\mathrm{W\,m^{-2}}$	$6.83\,\mathrm{W\,m^{-2}}$
			5.74 %	0.79 %	4.97 %
	SAT		ns	ns	ns
			ns	ns	ns
	Transpiration Efficiency		0.12 %	ns	0.10 %
			3.18 %	ns	2.70 %
	Canopy Temperature		−0.23 K	ns	ns
			−0.08 %	ns	ns
	GPP		$0.06\,\mathrm{Pg\,C\,yr^{-1}}$	ns	$0.06\,\mathrm{Pg\,C\,yr^{-1}}$
			1.18 %	ns	1.15 %
	Isoprene		$-1.04\,\mathrm{Tg\,C\,yr^{-1}}$	ns	$-0.86\,\mathrm{Tg\,C\,yr^{-1}}$
			−5.60 %	ns	−4.64 %
North-western	SW VIS Solar Radiation	Total	$-4.09\,\mathrm{W\,m^{-2}}$	$-2.18\,\mathrm{W\,m^{-2}}$	$-2.52\,\mathrm{W\,m^{-2}}$
Amazon Basin			−1.84 %	−0.98 %	−1.14 %
(73°–65°W; 5°S–5°N)		Direct	$-7.67\,\mathrm{W\,m^{-2}}$	$,-4.08\,\mathrm{W\,m^{-2}}$	$-4.80\,\mathrm{W\,m^{-2}}$
			−7.86 %	−4.17 %	−4.92 %
		Diffuse	$3.58\,\mathrm{W\,m^{-2}}$	$1.90\,\mathrm{W\,m^{-2}}$	$2.28\,\mathrm{W\,m^{-2}}$
			2.88 %	1.52 %	1.83 %
	SAT		−0.15 K	−0.28 K	−0.11 K
			−0.05 %	−0.09 %	−0.04 %
	Transpiration Efficiency		0.31 %	0.51	0.23 %
			3.20 %	5.19	2.31 %
	Canopy Temperature		−0.17 K	−0.31 K	−0.13 K
			−0.06 %	−0.10 %	−0.04 %
	GPP		$0.07\,\mathrm{Pg\,C\,yr^{-1}}$	$0.10\,\mathrm{Pg\,C\,yr^{-1}}$	$0.05\,\mathrm{Pg\,C\,yr^{-1}}$
			2.42 %	3.42 %	1.78 %
	Isoprene		ns	$0.37\,\mathrm{Tg\,C\,yr^{-1}}$	ns
			ns	2.39 %	ns

Table 5. Continued.

Region	Variable		SimCTRL − SimNOant	SimCTRL − SimNObb	SimCTRL − SimNOind
Central Africa	SW VIS Solar Radiation	Total	$-17.40\,\mathrm{W\,m^{-2}}$	$-14.41\,\mathrm{W\,m^{-2}}$	$-8.53\,\mathrm{W\,m^{-2}}$
(10°–25° E; 10° S–5° N)			$-8.68\,\%$	$-7.19\,\%$	$-4.25\,\%$
		Direct	$-24.80\,\mathrm{W\,m^{-2}}$	$-18.72\,\mathrm{W\,m^{-2}}$	$-10.75\,\mathrm{W\,m^{-2}}$
			$-34.85\,\%$	$-26.32\,\%$	$-15.12\,\%$
		Diffuse	$7.40\,\mathrm{W\,m^{-2}}$	$4.31\,\mathrm{W\,m^{-2}}$	$2.22\,\mathrm{W\,m^{-2}}$
			$5.72\,\%$	$3.33\,\%$	$1.72\,\%$
	SAT		$-0.19\,\mathrm{K}$	$-0.16\,\mathrm{K}$	$-0.08\,\mathrm{K}$
			$-0.06\,\%$	$-0.05\,\%$	$-0.03\,\%$
	Transpiration Efficiency		$0.28\,\%$	0.31	$0.14\,\%$
			$3.60\,\%$	4.06	$1.79\,\%$
	Canopy Temperature		$-0.23\,\mathrm{K}$	$-0.21\,\mathrm{K}$	$-0.11\,\mathrm{K}$
			$-0.08\,\%$	$-0.07\,\%$	$-0.04\,\%$
	GPP		$0.10\,\mathrm{Pg\,C\,yr^{-1}}$	$0.08\,\mathrm{Pg\,C\,yr^{-1}}$	ns
			$1.61\,\%$	$1.27\,\%$	ns
	Isoprene		$-0.55\,\mathrm{Tg\,C\,yr^{-1}}$	ns	$-0.30\,\mathrm{Tg\,C\,yr^{-1}}$
			$-1.89\,\%$	ns	$-1.02\,\%$

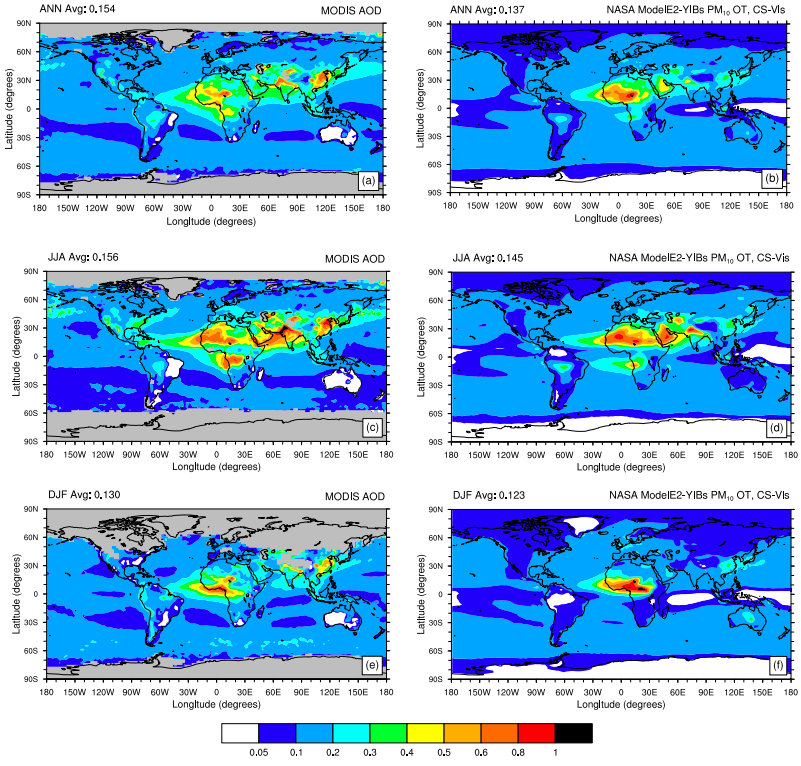

Figure 1. Annual and seasonal average coarse aerosol optical depth (AOD) seen by: **(a, c, e)** the MODIS instrument (at 550 nm; averaged over 2000–2007), and **(b, d, f)** NASA ModelE2-YIBs in the control present-day simulation ($\sim$ 2000s). Global mean values are given in the upper left corner of each map. Only boreal summer (JJA) and winter (DJF) seasonal averages are shown. For NASA ModelE2-YIBs, only clear-sky (CS) values in the visible (Vis) range are used to define $\mathrm{PM_{10}}$ optical thickness (OT).

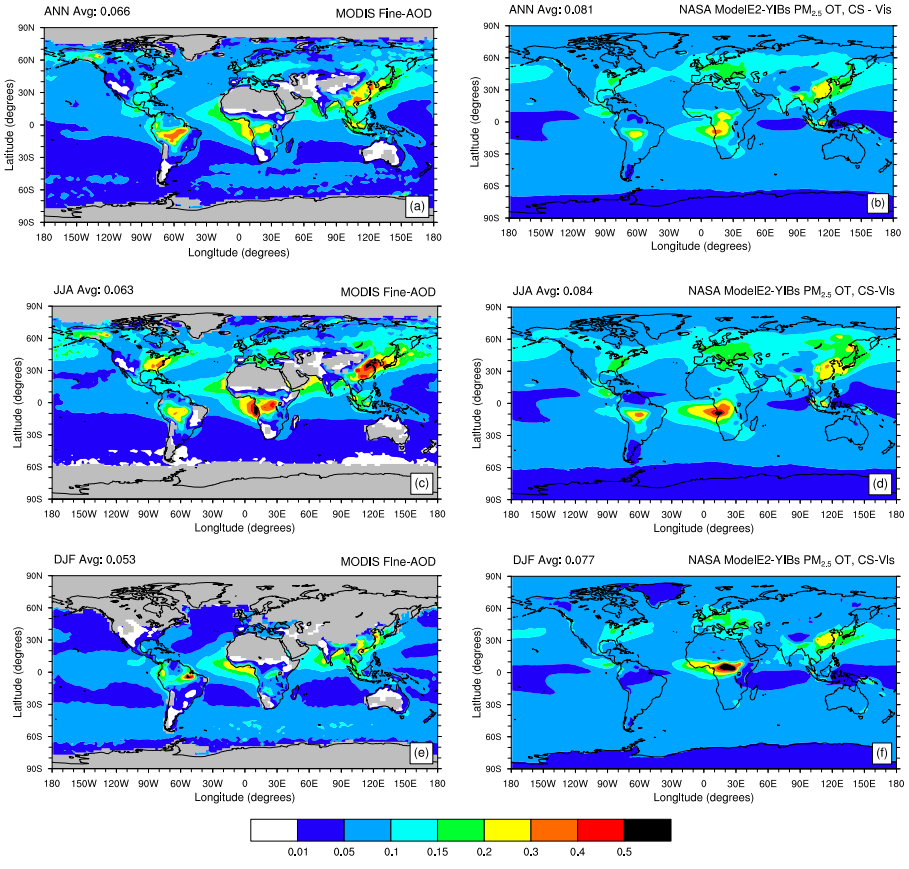

Figure 2. As Fig. 1 for fine-mode aerosol optical depth: **(a, c, e)** MODIS fine-AOD, and **(b, d, f)** model $\mathrm{PM}_{2.5}$ OT.

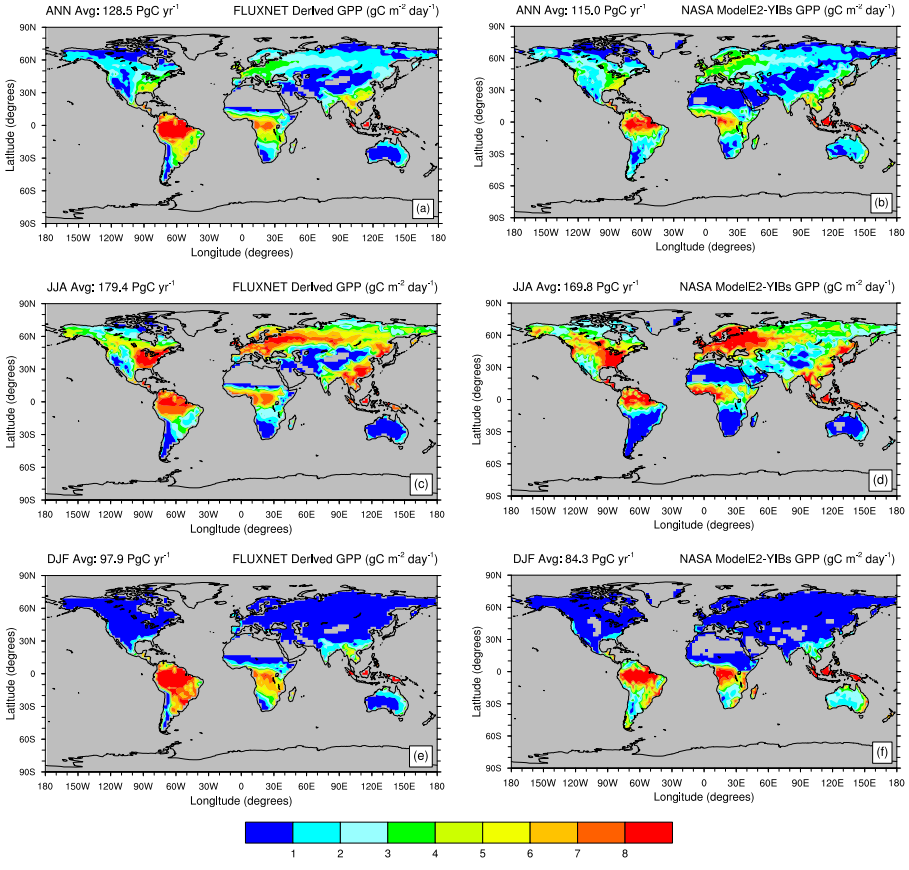

Figure 3. Annual and seasonal average gross primary productivity (GPP, in $\mathrm{g\,m^{-2}\,day^{-1}}$) as seen by: **(a, c, e)** a global FLUXNET-derived GPP product (averaged over 2000–2011), and **(b, d, f)** NASA ModelE2-YIBS in the control present-day simulation ($\sim$ 2000s). Global mean values are given in the upper left corner of each map. Only boreal summer (JJA) and winter (DJF) seasonal averages are shown.

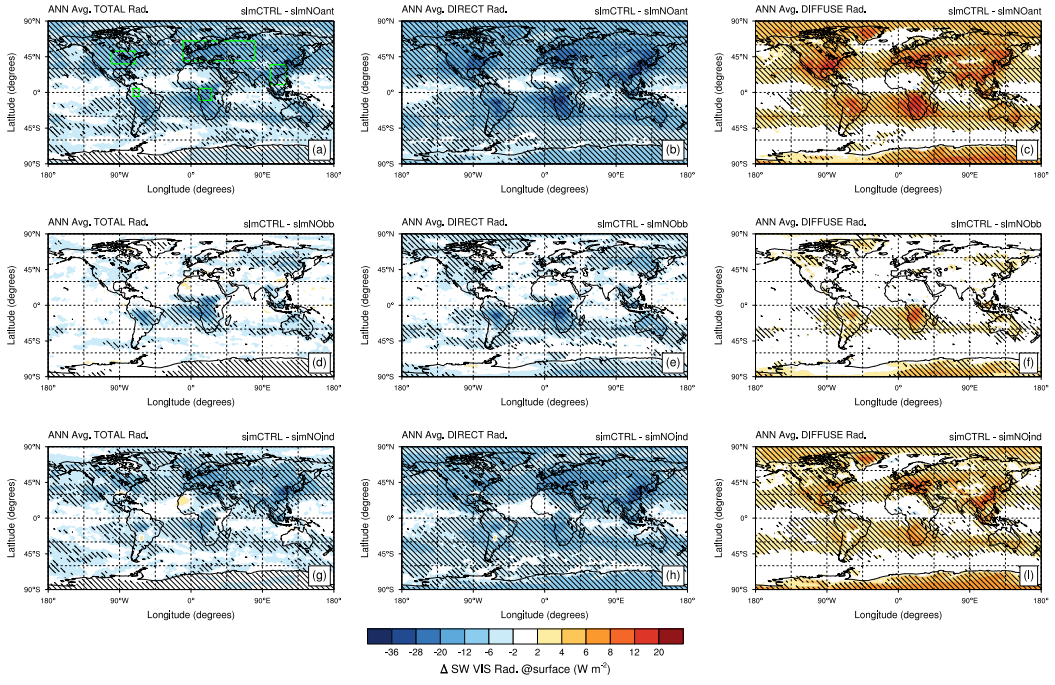

Figure 4. Spatial distribution of annual absolute change in short-wave visible (SW VIS) **(a, d, g)** total, **(b, e, h)** direct and **(c, f, i)** diffuse solar radiation (in $\mathrm{W\,m^{-2}}$). Changes are computed between the control experiment (SimCTRL) and sensitivity experiments: **(a–c)** without all anthropogenic emissions (SimNOant); **(d–f)** without biomass burning emissions (SimNObb); and **(g–i)** without anthropogenic emissions except biomass burning (SimNOind). The difference has been computed using last 20 year averages for each experiment. All experiments are set in a present-day climatic state. Shaded regions indicate areas where changes in solar radiation are significant at the 95 $\%$ confidence level. Green boxes on plot **(a)** highlight key regions selected for discussion.

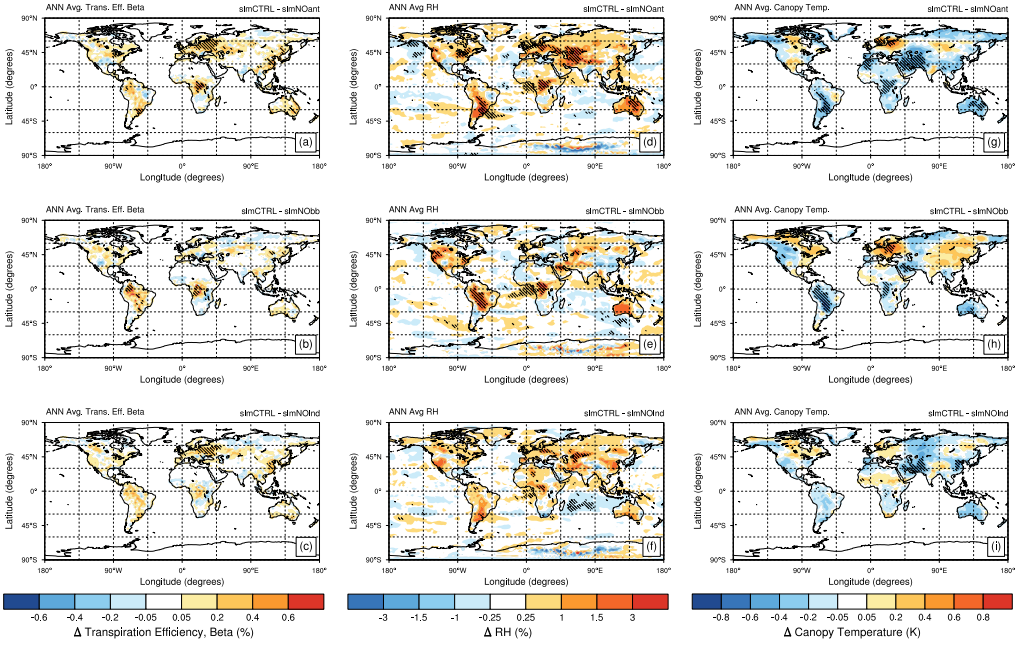

Figure 5. Spatial distribution of annual absolute change in transpiration efficiency, (beta, in %; left column panels), surface relative humidity (RH, in %; middle column panels) and canopy temperature (in K; right column panels) between the control experiment (SimCTRL) and sensitivity experiments: **(a, d, g)** without all anthropogenic emissions (SimNOant); **(b, e, h)** without biomass burning emissions (SimNObb); and **(c, f, i)** without anthropogenic emissions except biomass burning (SimNOind). The difference has been computed using last 20 year averages for each experiment. All experiments are set in a present-day climatic state. Shaded regions indicate areas where changes are significant at the 95 % confidence level.

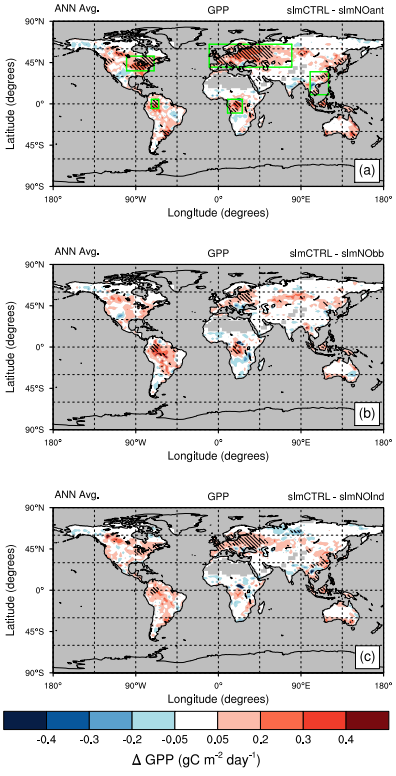

Figure 6. Spatial distribution of annual absolute change in Gross Primary Productivity (GPP, in $\mathrm{g\,C\,m^{-2}\,day^{-1}}$) between the control experiment (SimCTRL) and sensitivity experiments: **(a)** without all anthropogenic emissions (SimNOant); **(b)** without biomass burning emissions (SimNObb); and **(c)** without anthropogenic emissions except biomass burning (SimNOind). The difference has been computed using last 20 year averages for each experiment. All experiments are set in a present-day climatic state. Shaded regions indicate areas where changes in GPP are significant at the 95 % confidence level. Green boxes on plot **(a)** highlight key regions selected for discussion.

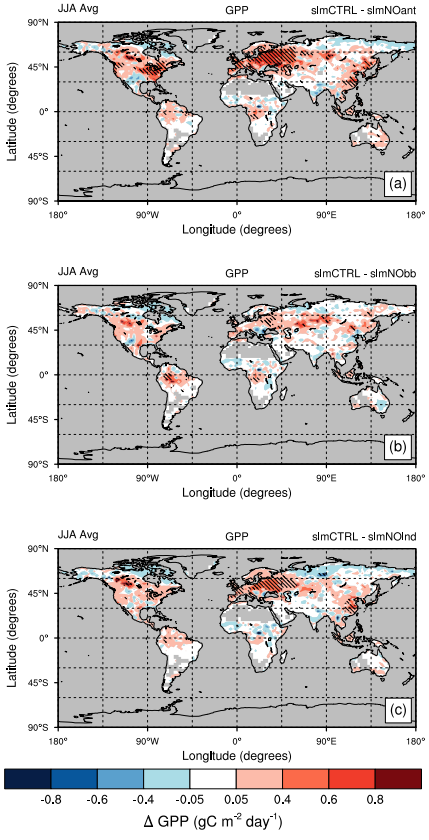

Figure 7. As Fig. 6 for seasonal (boreal summer, JJA) absolute change in Gross Primary Productivity (GPP, in $\mathrm{g\,C\,m^{-2}\,day^{-1}}$) between the control experiment (SimCTRL) and sensitivity experiments: **(a)** SimNOant, **(b)** SimNObb and **(c)** SimNOind.

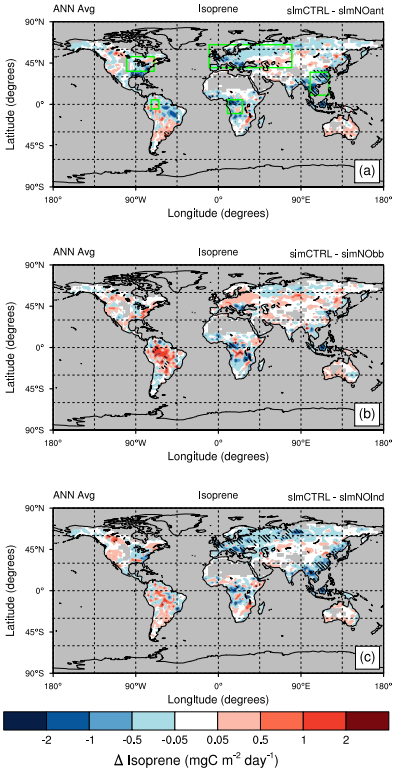

Figure 8. Spatial distribution of annual absolute change in isoprene emission (in $\mathrm{mg\,C\,m^{-2}\,day^{-1}}$) between the control experiment (SimCTRL) and sensitivity experiments: **(a)** without all anthropogenic emissions (SimNOant); **(b)** without biomass burning emissions (SimNObb); and **(c)** without anthropogenic emissions except biomass burning (SimNOind). The difference has been computed using last 20 year averages for each experiment. All experiments are set in a present-day climatic state. Shaded regions indicate areas where changes in isoprene emission are significant at the 95 $\%$ confidence level. Green boxes on plot **(a)** highlight key regions selected for discussion.